

# Detecting electromagnetic counterparts to LIGO/Virgo/KAGRA gravitational wave events with DECam: Neutron Star Mergers

K. Kunnumkai ,<sup>1</sup> A. Palmese ,<sup>1</sup> A. M. Farah ,<sup>2</sup> M. Bulla ,<sup>3,4,5</sup> T. Dietrich ,<sup>6,7</sup>  
P. T. H. Pang ,<sup>8,9</sup> S. Anand ,<sup>10</sup> I. Andreoni ,<sup>11</sup> T. Cabrera ,<sup>1</sup> and B. O'Connor ,<sup>1</sup>

<sup>1</sup>*McWilliams Center for Cosmology and Astrophysics, Department of Physics,  
Carnegie Mellon University, Pittsburgh, PA 15213, USA*

<sup>2</sup>*Department of Physics, University of Chicago, Chicago, IL 60637, USA*

<sup>3</sup>*Department of Physics and Earth Science, University of Ferrara, via Saragat 1, I-44122 Ferrara, Italy*

<sup>4</sup>*INFN, Sezione di Ferrara, via Saragat 1, I-44122 Ferrara, Italy*

<sup>5</sup>*INAF, Osservatorio Astronomico d'Abruzzo, via Mentore Maggini snc, 64100 Teramo, Italy*

<sup>6</sup>*Institut für Physik und Astronomie, Universität Potsdam,  
Haus 28, Karl-Liebknecht-Str. 24/25, 14476, Potsdam, Germany*

<sup>7</sup>*Max Planck Institute for Gravitational Physics (Albert Einstein Institute), Am Mühlenberg 1, Potsdam 14476, Germany*

<sup>8</sup>*Institute for Gravitational and Subatomic Physics (GRASP),  
Utrecht University, Princetonplein 1, 3584 CC Utrecht, The Netherlands*

<sup>9</sup>*Nikhef, Science Park 105, 1098 XG Amsterdam, The Netherlands*

<sup>10</sup>*Cahill Center for Astrophysics, California Institute of Technology, Pasadena CA 91125, USA*

<sup>11</sup>*Department of Physics and Astronomy, University of North Carolina at Chapel Hill, Chapel Hill, NC 27599-3255, USA*

With GW170817 being the only multimessenger gravitational wave (GW) event with an associated kilonova (KN) detected so far, there exists a pressing need for realistic estimation of the GW localization uncertainties and rates, as well as optimization of available telescope time to enable the detection of new KNe. For this purpose, we simulate GW events assuming a data-driven, GW-motivated distribution of binary parameters for the LIGO/Virgo/KAGRA (LVK) fourth and fifth observing runs (O4 and O5). We map the binary neutron star (BNS) and neutron star-black hole (NSBH) properties to the optical light curves arising from r-process nucleosynthesis in the ejecta. We use the simulated population of KNe to generate follow-up observing plans, with the primary goal of optimizing detection with the Gravitational Wave Multi-Messenger Astronomy DECam Survey (GW-MMADS). We explore the dependence of KN detectability on the mass, distance, inclination, and spin of the binaries. Assuming that no BNS was detected during O4 until the end of 2024, we present updated GW BNS (NSBH) merger detection rates:  $\sim 1 - 9$  ( $2 - 9$ )  $\text{yr}^{-1}$  in O4, and  $13 - 110$  ( $18 - 110$ )  $\text{yr}^{-1}$  in O5. Of these events, we expect to detect BNS (NSBH) KNe with DECam at a per year rate of: 0 – 2 (0) in O4, and 2 – 28 (0 – 3) in O5, conditional on the uncertainty on the equation of state (EOS) and volumetric rates of the mergers. We expect the majority of BNS detections and also those accompanied by a detectable KN to produce a hypermassive NS remnant, with a significant fraction of the remaining BNSs promptly collapsing to a BH. We release our GW simulations and the depths needed to detect a significant fraction of simulated KNe to enable the astronomical community to use them in their multimessenger campaigns and analyses.

## I. INTRODUCTION

In 2017, a binary neutron star (BNS) merger event was detected in gravitational waves (GWs), GW170817 [2], and it was accompanied by multiple electromagnetic (EM) counterparts [68]. The detection of its EM counterparts, namely the gamma-ray burst GRB 170817A [4], the kilonova (KN) AT2017gfo [38, 103], and later the afterglow [44, 70], opened a new era of multimessenger astronomy [73].

Kilonovae [75] are transients ranging from the infrared to the ultraviolet powered by the radioactive decay of heavy nuclei synthesized in the highly-neutronized material ejected during neutron star (NS) mergers. These transients are considered to provide smoking-gun evidence for BNS or neutron star-black hole (NSBH) mergers. The detection of the KN AT2017gfo enabled hundreds of multimessenger analyses on the theory of gravity [23], the Universe's expansion [3, 30, 52, 84], the formation and fate of compact objects [26, 61, 85, 104], thanks to its precise localization in the sky, which allowed us to pinpoint the host galaxy of the GW merger. Moreover, KN observations themselves provide us with information on the physics of NS mergers, including but

not limited to their composition [15, 40, 53, 102, 105, 106], EOS [36, 39, 72, 89], fate of the remnant object [107] and origin of heavy elements (generated by r-process nucleosynthesis in the neutron-rich ejecta of the KNe [57]). The wide variety of possible multimessenger analyses from the identification of a KN motivates us to optimize the follow-up of BNS and NSBH merger events to characterize multimessenger sources beyond GW170817.

Currently, the international GW network consisting of the advanced LIGO [55], advanced Virgo [11], and KAGRA [13] interferometers (LVK) is carrying out its fourth observing run (O4). Although the LVK detected a few BNS [5] and NSBH [8, 9] candidates at different confidence levels in O3, there has been no single multi-messenger KN detection since the second observing run (O2) [14, 16, 48]. This is despite the improved detector sensitivity beyond O2, which should lead to a larger number of NS merger detections with an increased signal-to-noise ratio. Despite the fact that EM counterparts other than KNe have been claimed to be associated with GW events [49, 77], their association is uncertain [17, 24, 69, 83, 91, 101]. The lack of KN detections can mainly be attributed to both NS merger rates likely to be at the

lower end of the ranges previously estimated in [55], the lack of Virgo operations during the first part of O4, and, related to this point, the greater uncertainty in the sky localization of NS mergers from GWs than what was predicted in forecasts including Virgo and often KAGRA (see, e.g., [33, 87, 96]). This calls for a more realistic estimation of the localization uncertainties of NS mergers and a revised observing strategy to follow up events. To support such efforts, observing scenarios are simulated to accurately predict the source localization and detection of GW events.

In this work, we make end-to-end simulations of GW events during the current O4 run and the upcoming O5 run (expected to start in 2027) using updated LIGO/Virgo/KAGRA (LVK) detector sensitivities to assess the ability of the network to reconstruct the sky localization of the source and to accurately forecast the detection rates of EM counterparts. Moreover, we make use of the latest data-driven population for the GW source properties to inject mergers into our simulations [41]. This ensures that the important features in the mass and spin distributions of black holes (BHs) and NSs are properly incorporated in the simulations, since these can have a significant effect on the EM counterpart detectability. First, since the astrophysical GW population of NSs in BNS and NSBH mergers possibly shows a broader and flatter mass distribution than observed from EM observations in the Milky Way [10], and because the mass of the binary components has a strong impact on the KN ejecta properties, taking into account the GW population to the best of our knowledge is essential to optimize our follow-up strategy of both BNS and NSBH mergers. Second, the mass distribution of [41] allows for a dip between the expected NS and BH mass distributions, which is not necessarily an empty gap, hence it can accommodate objects such as those in GW190814 [7]. A population model that takes into account objects in the gap may result in a more promising scenario for multi-messenger kilonova detections from NSBHs [1, 63] than was previously thought [25]. We then compute KN light curves for each modeled BNS and NSBH mergers and develop follow-up strategies based on the KN magnitude distributions.

The simulations we present here are publicly available at [64]<sup>1</sup> and will allow the astronomical community to accurately plan observation programs to minimize wastage of precious telescope time. Specifically, we consider the case of optimizing EM counterpart searches for one of the most powerful optical-to-near-infrared instruments currently available to follow up GW events, the Dark Energy Camera (DECam; [43]). This is designed for our survey GW-MMADS (Gravitational Wave Multi-Messenger Astronomy DECam Survey; Proposal ID: 2023B-851374; PIs: Andreoni & Palmese [31]) which is carrying out follow up of GW events during O4. This is an effort to complement previous works [27, 33, 55, 58, 60, 87, 96] in various ways, namely by taking into account the reduced Virgo sensitivity compared to what was previously considered for O4, by considering a specific

follow-up campaign, accounting for uncertainties in the inference of the mass distribution of compact binary mergers, and employing different KN models.

This paper is structured as follows: in Section II, we describe the methods used to produce the simulations for the O4 and O5 runs, to attach simulated KNe lightcurves to the GW events and to schedule simulated follow-up campaigns of the events. In Section III, we discuss the results of our simulation runs as well as the KN detection efficiency with our fiducial strategy, and its dependence on various binary parameters. We present our discussion and conclusion in Section IV and V respectively.

## II. METHODOLOGY

### A. Simulation of GW Signals

We produce realistic simulations of GW events with LVK O4 and O5 sensitivities. We use BAYESTAR, a rapid sky localization code to localize the mergers in sky and distance [99, 100], tools from LALSuite [66] to make simulations of GW events and the public software `ligo.skymap` to generate and visualize the GW skymaps. We make 3 different simulations. Both simulation 1 and simulation 2 assume LIGO detectors at O4 sensitivity, but the latter assumes Virgo at O3 sensitivity in addition to the LIGO detectors. For simulation 3, we use all LVK detectors at the expected O5 sensitivity.

Simulation number	Observing Network run	BNS	NSBH
1	O4	HL	678 932
2	O4	HLV	825 1116
3	O5	HLVK	1791 2719

TABLE I. Number of detected BNS and NSBH mergers from different simulations out of the  $10^5$  compact binary coalescence (CBC) drawn from the distribution of [41]. For simulation 1, we used the LIGO detectors at O4 sensitivity, simulation 2 consists of the Virgo detector at O3 sensitivity in addition to the LIGO detectors at O4 sensitivity, whereas simulation 3 has all LVK detectors at O5 sensitivity. H, L, V, and K stands for LIGO Hanford, LIGO Livingston, Virgo, and KAGRA detectors, respectively.

The mass and spin distributions are chosen as described in the POWER LAW + DIP + BREAK (PDB) model [10, 41, 42]. It assumes a broken power law in mass with a notch filter to enable a mass gap between  $\sim 2-8 M_\odot$  that is allowed to vary in depth. The model also adds a low-pass filter to the upper end of the BH mass to allow for possible tapering of the mass distribution. The masses of both components (i.e. primary and secondary mass,  $m_1$  and  $m_2$ ) are described by this functional form, and a pairing function is employed to account for the fact that, within a given binary, the components' masses tend to be similar.

Draws are taken from the hyper-posterior of the PDB model fit to the third GW Transient Catalog (GWTC-3; [67]). These

<sup>1</sup> <https://zenodo.org/records/14207687>

hyper-posterior draws describe the probability of obtaining a system with masses  $m_1$  and  $m_2$ :  $p(m_1, m_2)$ . The masses are then drawn from  $p(m_1, m_2)$ . Note that this differs from the population assumed in [60], although that work also employed the PDB model: here we take into account the uncertainties in the population inference as we consider the full population posterior, effectively marginalizing over these uncertainties, instead of assuming a fixed population from the maximum *a posteriori* parameters. This is especially important for EM-bright NSBHs as the PDB posterior mode from GWTC-3 happens to have a nearly empty mass gap, but the uncertainties on the depth and location of the gap are large, so that considering the entire range of possibilities allowed by the data may have a significant impact.

Our model additionally assumes an isotropic orientation and a uniform magnitude for component spins. Objects with a mass less than  $2.5 M_\odot$  have spin magnitudes in the range  $[0, 0.4]$ , while objects with higher masses have spins defined as in the range  $[0, 1]$ . As described in Abbott et al. [10], these spin ranges were established by the sensitivity estimates available in GWTC-3.

We draw  $10^5$  CBCs from a sample following the PDB model. We draw the masses and spins of the CBCs from the distribution described above, uniformly distribute the samples in comoving volume, and isotropically distribute them in the orbital orientation and sky location. We follow [87] and assess the detectability of GW events with an individual detector and network signal-to-noise ratio (SNR) thresholds of 1 and 8, respectively, for the population of NS mergers. If at least one of the detectors detects the signal above these thresholds, it is counted as a GW event. We use a duty cycle of 70% for each detector and employ a Gaussian filter to recover the signal from the noise. The statistics of the sources detected, grouped by subpopulation, are shown in table I. The noise power spectral density (PSD) curves are considered for each detector per observing run. For the LIGO network at O4 sensitivity, we use the PSD curve aligo\_O4high.txt [6], and for the Virgo detector at O3 sensitivity, we use avirgo\_O3actual.txt [6]. For the O5 run, we assume an A+ sensitivity for the LIGO detectors, avirgo\_O5low\_NEW.txt for Virgo and kagra\_128Mpc.txt for KAGRA respectively, all from <https://dcc.ligo.org/LIGO-T2000012-v1/public>.

The distribution we use does not rely on binary classification, allowing us to define mass ranges for the three astrophysical sub-populations in which we are interested: BNSs, NSBHs, and binary black holes (BBHs). The maximum mass of a non-rotating NS  $M_{\text{TOV}}$  is calculated using the Tolman-Oppenheimer-Volkoff (TOV) limit [56], which according to the maximum posterior EOS from [54] assumed in this work is  $2.436 M_\odot$ . A rotating NS can exceed this limit. To account for this, we compute the maximum mass the components can have in each BNS and NSBH systems based on the spin  $a$  of each component, using the equation given in [28, 78]:

$$M_{\max}(a, a_{\text{Kep}}, M_{\text{TOV}}) = M_{\text{TOV}} \left( 1 + A_2 \left( \frac{a}{a_{\text{Kep}}} \right)^2 + A_4 \left( \frac{a}{a_{\text{Kep}}} \right)^4 \right) \quad (1)$$

where  $A_2 = 0.132$ ,  $A_4 = 0.071$  and for our fiducial EOS the

dimensionless spin at the mass shedding limit is  $a_{\text{Kep}} = 0.606$ , and it is defined in [28, 78]:

$$a_{\text{Kep}} = \frac{\alpha_1}{\sqrt{C_{\text{TOV}}}} + \alpha_2 \sqrt{C_{\text{TOV}}} \quad (2)$$

Here  $\alpha_1 = 0.045$ ,  $\alpha_2 = 1.112$  and  $C_{\text{TOV}}$  is related to the TOV mass and radius by the equation  $C_{\text{TOV}} = \frac{M_{\text{TOV}}}{R_{\text{TOV}}}$ . For the purposes of classification, we use the maximum NS mass  $M_{\max}$  defined in Eq. (1). Labeling the more massive object in each system as  $m_1$  and the less massive object as  $m_2$ , the BNS systems are then binaries with  $m_1, m_2 < M_{\max}$ , NSBH are those with  $m_2 < M_{\max}$  and  $m_1 \geq M_{\max}$ . In what follows, we also explore the detectability of KN assuming the lower and upper 95% credible intervals of the EOS constraints from [54], hereafter referred to as softer and stiffer EOS, to assess the impact of the EOS on our results.  $M_{\text{TOV}}$  for softer, fiducial and stiffer EOSs used in this work are  $2.069 M_\odot$ ,  $2.436 M_\odot$  and  $2.641 M_\odot$  respectively.

## B. Simulation of EM Counterparts

For modeling KN light curves from BNS and NSBH mergers, we use the Bu2019lm and Bu2019nsbh surrogate models implemented in the Nuclear physics and MultiMessenger Astronomy (NMMA; [39, 86]) framework. These models are constructed from KN grids computed with the time-dependent three-dimensional Monte Carlo radiative transfer code POSSIS [29] for BNS [39] and NSBH [14] mergers, and allow us to simulate KN light curves for arbitrary combinations of the BNS and NSBH binary parameters.

The main outflow properties to model a KN with the aforementioned models are the dynamical ejecta mass ( $M_{\text{dyn}}$ ) and the disk wind ejecta mass ( $M_{\text{wind}}$ ). Dynamical ejecta are launched during the merger due to hydrodynamical forces that squeeze the material at the interface between the merging objects [21, 50], while the wind ejecta originate from the disk of material accreted around the central remnant. The relative importance of these processes depends on the parameters of the binary such as the total mass, mass ratio ( $q = m_2/m_1$ ) and the EOS, with asymmetric mass-ratio systems ( $q \ll 1$ ) typically leaving significantly larger amounts of unbound material than more symmetric mass-ratio binaries in BNS systems [21].

For BNS mergers,  $M_{\text{dyn}}$  depends on the compactness of the merging stars and their mass ratio. We follow the relation from [62] to model  $M_{\text{dyn}}$

$$\frac{M_{\text{dyn}}^{\text{BNS}}}{10^{-3}} = \left( \frac{a}{C_1} + b \left( \frac{m_2}{m_1} \right)^n + c C_1 \right) m_1 + (1 \leftrightarrow 2). \quad (3)$$

Here,  $C_1 = Gm_1/R_1c^2$  and the best-fit parameters from [62] are  $a = -9.3335$ ,  $b = 114.17$ ,  $c = -337.56$  and  $n = 1.5465$ . The residuals about their best fit follow a Gaussian distribution with a standard deviation of  $\sigma = 0.004 M_\odot$ , with  $M_{\text{dyn}}^{\text{BNS}}$  being truncated at zero (no negative values allowed). We therefore add an uncertainty in ejecta mass  $\alpha$  to the fitting formula to account for this. Such uncertainties arise from the limited

Network	Binary type	$A < 10^3 \text{ deg}^2$	$A < 500 \text{ deg}^2$	$A < 100 \text{ deg}^2$	$A < 10 \text{ deg}^2$	$V_{90} < 10^3 \text{ Mpc}^3$	$A_{90,\text{median}} (\text{deg}^2)$	$V_{90,\text{median}} (10^6 \text{ Mpc}^3)$	$D_{\text{median}} (\text{Mpc})$
HL O4	BNS	21.6%	8.8%	1.0%	0%	0.1%	1822	19	259
	NSBH	18.9%	7.8%	0.9%	0%	0%	2136	83	380
HLV O4	BNS	28.5 %	14.6%	3.8%	0.5%	0.5%	1658	23	277
	NSBH	26.6%	14.9%	4.7%	0.6%	0.2%	1915	91	409
HLVK O5	BNS	37.2%	25.9%	13.0%	2.9%	0.5%	1701	217	614
	NSBH	38.9%	28.0%	14.5%	3.4%	0.4%	1714	585	884

TABLE II. Percentage of events with localization precision below a given threshold, for the different network configurations considered.

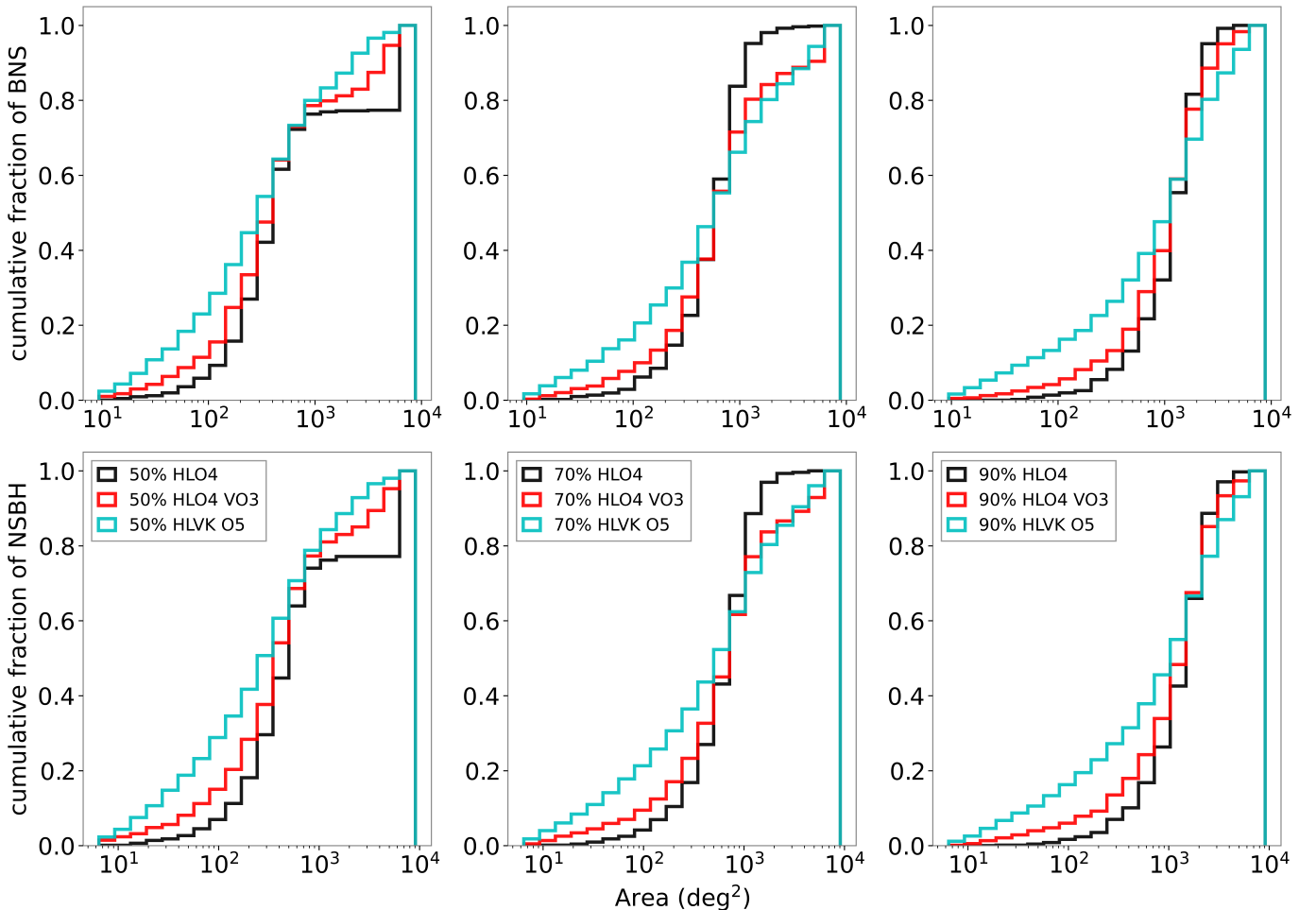


FIG. 1. Cumulative distribution of area at 50, 70, and 90% credible intervals for simulations 1 (black line), 2 (red line), and 3 (blue line) for BNS (top) and NSBH (bottom) events.

coverage of the parameter space by existing numerical simulations, but also from ignoring or approximating some important physics [62], e.g., neutrino radiation.

The disk mass for BNS mergers depends on the total mass and the threshold mass  $M_{\text{th}}$  (which is the limiting total binary mass  $M_{\text{tot}}$  beyond which the BNS system would undergo prompt collapse into a BH [12, 20]), and follows the relation

from [39]:

$$\log_{10}(M_{\text{disk}}^{\text{BNS}}) = \max \left( -3, a \left( 1 + b \tanh \left[ \frac{c - M_{\text{tot}}/M_{\text{th}}}{d} \right] \right) \right). \quad (4)$$

Here,  $M_{\text{th}} = k_{\text{th}} M_{\text{TOV}}$  [51] where  $k_{\text{th}}$  is a function of  $M_{\text{TOV}}$  and the EOS [20],  $a$  and  $b$  are functions of the mass ratio  $q$

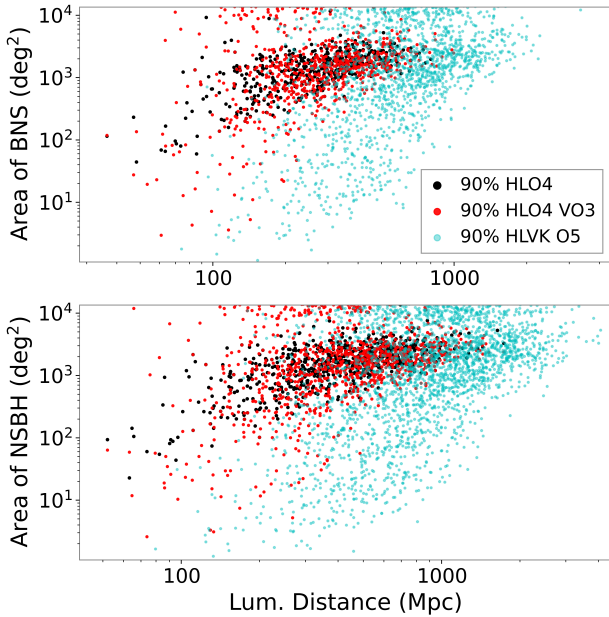


FIG. 2. 90% CI area versus luminosity distance for BNS (top) and NSBH (bottom) events with the same color scheme as in Figure 1.

and given by:

$$\begin{aligned} a &= a_0 + \delta_a x_i \\ b &= b_0 + \delta_b x_i \\ x_i &= 0.5 \tanh(\beta(q - q_t)) \end{aligned} \quad (5)$$

where  $a_0 = -1.581$ ,  $b_0 = -0.538$ ,  $c = 0.953$ ,  $d = 0.0417$ ,  $\delta_a = -2.439$ ,  $\delta_b = -0.406$ ,  $\beta = 3.910$ , and  $q_t = 0.900$ . The fraction of disk mass ejected as wind is given by the parameter  $\zeta$ , which, when multiplied by  $M_{\text{disk}}^{\text{BNS}}$ , gives  $M_{\text{wind}}^{\text{BNS}}$ . Although the true value of  $\zeta$  is unknown [79], we draw from a Gaussian centered at 0.3 with a standard deviation  $\sigma$  of 0.15; cf. Sec. 2.2 of [90] for a more detailed discussion.

For NSBH mergers,  $M_{\text{dyn}}$  is a function of the mass of the components, their spins, the baryonic mass of NS  $M_{\text{NS}}^b$ , and the compactness of the secondary component. It is given by the equation from [62]:

$$\frac{M_{\text{dyn}}^{\text{NSBH}}}{M_{\text{NS}}^b} = a_1 Q^{n_1} \frac{1-2C_{\text{NS}}}{C_{\text{NS}}} - a_2 Q^{n_2} \frac{R_{\text{ISCO}}}{m_1} + a_4, \quad (6)$$

where the best fitting parameters are  $a_1 = 0.007116$ ,  $a_2 = 0.001436$ ,  $a_4 = -0.02762$ ,  $n_1 = 0.8636$ , and  $n_2 = 1.6840$ . Here,  $Q = m_1/m_2$  and  $R_{\text{ISCO}}$  is the radius of the innermost stable circular orbit (ISCO) of the BH with mass  $m_1$  and spin  $\chi_{\text{BH}}$ . The baryonic mass of the NS is given by  $M_{\text{NS}}^b = m_2 \left( 1 + \frac{0.6C_{\text{NS}}}{1-0.5C_{\text{NS}}} \right)$

[65]. Again, negative values of  $M_{\text{dyn}}^{\text{NSBH}}$  are assumed to be zero. In our simulations, we add the uncertainty on the dynamical ejecta mass  $\alpha$ , which is a truncated Gaussian with  $\mu = 0$  and  $\sigma = 0.0047$  [62].

For NSBH mergers, the remnant mass, which is used to refer to the baryon mass outside the BH  $\sim 10$  ms post-merger, is

calculated using the component masses, spins, and compactness of the NS from the fitting formula by [45]:

$$\hat{M}_{\text{rem}}^{\text{NSBH}} = \left[ \max \left( a \frac{1-2C_{\text{NS}}}{\eta^{1/3}} - b R_{\text{ISCO}} \frac{C_{\text{NS}}}{\eta} + c, 0 \right) \right]^{1+d}. \quad (7)$$

Here,  $\eta = Q/(1+Q^2)$  is the symmetric mass ratio,  $\hat{M} = M_{\text{rem}}^{\text{NSBH}}/M_{\text{NS}}^b$ , and  $a = 0.40642158$ ,  $b = 0.13885773$ ,  $c = 0.25512517$ ,  $d = 0.761250847$ . The disk mass  $M_{\text{disk}}^{\text{NSBH}}$  is calculated by subtracting  $M_{\text{dyn}}^{\text{NSBH}}$  from  $\hat{M}_{\text{rem}}^{\text{NSBH}}$ . Of course, if the remnant mass is zero, this also corresponds to no tidal disruption. We draw  $\zeta$  from a Gaussian centered at 0.3 with width  $\sigma = 0.15$ , and multiply it by  $M_{\text{disk}}^{\text{NSBH}}$  to obtain the wind ejecta mass  $M_{\text{wind}}^{\text{NSBH}}$ . Following [18, 74] we further require  $M_{\text{dyn}}$  to be less than 50% of  $M_{\text{rem}}$ , to be consistent with results found by numerical simulations. For both BNS and NSBH mergers, an ejecta mass cut-off point of  $10^{-5} M_{\odot}$  was used to consider the KN as produced. For NSBH mergers we further consider a cut at  $10^{-3} M_{\odot}$  when generating the lightcurves. This is to avoid extreme extrapolations of the Bu2019nsbh surrogate models since the original grid from POSSIS is computed down to  $10^{-2} M_{\odot}$  for both components ( $M_{\text{dyn}}$  and  $M_{\text{wind}}$  run from 0.01 to  $0.09 M_{\odot}$  with a step of  $0.01 M_{\odot}$  [14]). For BNSs this is not a problem because the vast majority of sources produce ejecta with mass above the grid limit for Bu2019lm ( $M_{\text{dyn}} \in [0.001, 0.005, 0.01, 0.02] M_{\odot}$  and  $M_{\text{wind}}$  runs from 0.01 to  $0.13 M_{\odot}$  with a step of  $0.04 M_{\odot}$  [39]).

We use these outflow properties to simulate KNe lightcurves for all BNS and NSBH events in  $u, g, r, i, z, y$  bands. For  $g$  and  $i$  bands, we check whether the simulated KN is detectable for those events for which the pointings covered by our observing plans matches the true sky location of the event. This provides an estimate of the KNe that can be detected in these 2 bands using DECam during the O4 and O5 runs. Here, detection means at least one observation in the simulated lightcurve is above the  $5\sigma$  depth. We use AB magnitudes throughout our work.

### C. Simulated Observing Strategy

We consider the case of optimizing EM counterpart searches for DECam, however, most of our results can be applied to other instruments with similar filters. DECam is a wide-field high-performance CCD camera mounted on the 4m Blanco Telescope at Cerro-Tololo Inter-American Observatory in Chile. We take DECam to have a base sensitivity of 24.3 AB mag in  $g$ -band and 23.9 AB mag in  $i$ -band (at  $5\sigma$  depth at 7 days from new Moon) for our fiducial strategy. To simulate follow-up observations, we use the Gravitational-Wave Electromagnetic Optimization code (gwemopt; [35, 37]) with DECam tiling.

We calculate the exposure time (ET) in  $g$  and  $i$  bands ( $\text{ET}_g$  and  $\text{ET}_i$  respectively) as the time needed to reach a  $5\sigma$  depth at the magnitude given by the 90th quantile of the KN magnitudes in our simulations. We use magnitudes at 1 day from the merger for BNS events and at 2 days from the merger for NSBH events since this is when the KN magnitude peaks.

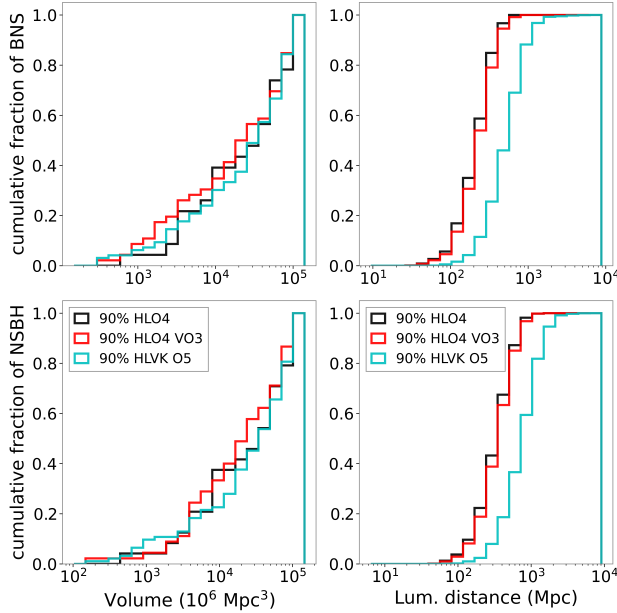


FIG. 3. Cumulative distribution of volume and distance for BNS (top) and NSBH (bottom) at 90% credible intervals for the 3 simulations using the same color scheme as in Figure 1.

This is done in bins of luminosity distance. For the calculated exposure times, we then compute the number of tiles  $N_t$  that can be observed as:

$$N_t = \frac{4 \text{ hours}}{ET_g + ET_i + 60 \text{ seconds}}, \quad (8)$$

where we assume a maximum observing time of 4 hours and a telescope overhead time of 60s (30s per exposure). This simulated follow-up requires the airmass to be less than 2.2, and factors including the field of view and sensitivity of the telescope are taken into consideration. Our final goal is to use the simulations to choose an ideal observing time that is not necessarily similar to that of what we consider our fiducial strategy throughout this work, but that maximizes our chances of detecting a KN at a specific distance.

### III. RESULTS

#### A. GW Localizations and rates

In this work, we focus on the results for BNS and NSBH mergers from our simulations, although binary black hole simulations are also produced. Since the GW source localization is determined by the sky area and the comoving volume contained within some probability, as well as the luminosity distance, we show cumulative distributions of these quantities for the different simulations considered in Figure 1. The median localization volume is of the order of  $10^7 \text{ Mpc}^3$  for O4 simulations and of the order of  $10^8 \text{ Mpc}^3$  for O5 simulation.

Median area and distance are of the order of  $10^3 \text{ deg}^2$  and a few hundred Mpc respectively as shown in Table II.

We also report the percentage of well-localized events (based on area and volume) in Table II. As expected, the inclusion of Virgo even at the sensitivity of O3 results in the detection of a higher number of well-localized events at distances  $< 100 \text{ Mpc}$ , as can also be seen in Figure 2 based on area, and in Figure 3 based on localization volume. For example, events with 90% CI area within 100 sq. deg. see a four-fold increase in numbers with the inclusion of Virgo. This is in part because increasing the number of detectors would positively impact event localization due to the slight difference in arrival time of the signal. This is crucial for typical follow-up campaigns, which may focus on the better localized events by imposing a cut in area. Less distant events produce higher SNRs and, therefore, smaller localization regions compared to further events with the same chirp mass. Thus, as we go to larger areas, we probe more distant events, making the improvement in localization less prominent. For O4 with Virgo we find that events localized to within 100 sq. deg. occur at distances  $< 220 \text{ Mpc}$  ( $< 480 \text{ Mpc}$ ), while those localized to  $< 500 \text{ sq. deg.}$  occur at distances  $< 350 \text{ Mpc}$  ( $< 590 \text{ Mpc}$ ) for BNS (NSBH).

Compared to the two O4 detector configurations, the O5 network detects events out to larger distances and detects a larger number of well-localized events, both in terms of area and volume. As expected, due to the larger distances of most detections, the median area and volume of events appear larger than or similar to O4, despite the growing number of detectors. In O5, events localized to within 100 sq. deg. occur at distances  $< 950 \text{ Mpc}$  ( $< 1400 \text{ Mpc}$ ), while those localized to  $< 500 \text{ sq. deg.}$  occur at distances  $< 1100 \text{ Mpc}$  ( $< 2400 \text{ Mpc}$ ).

We assume a volumetric merger rate of  $170_{-120}^{+270} \text{ yr}^{-1} \text{ Gpc}^{-3}$  for BNSs, and  $27_{-17}^{+31} \text{ yr}^{-1} \text{ Gpc}^{-3}$  for NSBHs, following the merger rates in Table II of [32], where NS and BHs in this case are delineated at  $2.5 M_\odot$ . We expect  $\sim 2-20$  ( $\sim 2-9$ ) BNS (NSBH) detections per year in O4, and  $28-260$  (18-110) BNS (NSBH) detections per year in O5. These rates are obtained based on observations during the first three observing runs. We update these predictions assuming preliminary rates based on the assumption that no BNS merger has been detected during O4. This assumption relies on the fact that no high-significance BNS alert has been issued in O4 up to the end of 2024. Following the public LVK alerts User Guide<sup>2</sup>, one can estimate the surveyed time-volume during the first part of O4 (O4a) as 0.85 times that surveyed by the previous runs, and over  $\sim 260$  days in 2024 that fraction becomes  $\sim 1.35$ . The previous runs ranges and time fractions are retrieved from the Gravitational Wave Open Science website.<sup>3</sup> For O4b, such information is not yet publicly available so detectors' ranges are based on their performance preceding the start of O4b, and the time fractions are assumed to be the same

<sup>2</sup> <https://emfollow.docs.ligo.org/userguide/capabilities.html#probability-of-the-detection-of-bns-and-nsbh-mergers-in-o4b>

<sup>3</sup> <https://gwosc.org/>

as in O3b. Following this, the updated 90% CI rate interval for BNSs in the PDB model becomes  $27 - 240 \text{ yr}^{-1} \text{Gpc}^{-3}$  based on O4a or  $22 - 190 \text{ yr}^{-1} \text{Gpc}^{-3}$  based on O4b until the end of 2024. Therefore, our preliminary GW BNS detection rates based on the non-detections up to the end of 2024 are  $\sim 1 - 9 \text{ yr}^{-1}$  for O4 and  $13 - 110$  for O5. See XI in Appendix A for our GW BNS detection rates and kilonova detectability taking into account non-detection of BNS mergers in O4a alone.

In Table II we also report the fraction of events with a volume localization of  $< 1000 \text{ Mpc}^3$ , corresponding to a volume within which we expect to find less than one galaxy cluster ( $\sim 0.1$  based on [94]) with halo mass  $\gtrsim 10^{13.5} M_\odot$ . This is interesting because short gamma-ray bursts have also been observed to occur in galaxy clusters (e.g., [81]), and GW170817 occurred in a galaxy group. Although such well-localized events are extremely rare, it is possible that one of these could be observed in O5 given the yearly detection rates combined with the potentially long (few-year) duration of O5.

## B. Kilonova Detectability

In what follows, we explore the KN detectability dependence on various binary observables in order to inform our follow-up strategy. At first, we do not consider coverage by `gwemopt` (which is considered in the next subsection); but rather we consider the event as detectable if the KN lightcurve in a given filter is brighter than the DECam detection limit (24.3 mag in *g*-band and 23.9 mag in *i*-band for the fiducial exposure time). We choose to show the results from the O5 simulations in the figures as these include a larger number of objects, and the corresponding O4 plots would be mostly repetitive. Note that in what follows, O4 is used to denote simulation 2 and O5 is used to denote simulation 3. Two quantities that can typically be easily constrained from the GW data are chirp mass or total mass and distance, so we start by focusing on combinations of these parameters.

### 1. Total mass dependence

In Figure 4 we show the total mass versus luminosity distance for all events that we classify as BNS (left) or NSBH (right) in our O5 simulations. The entire population of BNSs and NSBHs detected in GWs is shown by yellow squares. The blue squares indicate the subsample of objects that produce a KN according to our model. Of the ones that produce a KN, detection in *g* and *i*-bands are shown by a black point and a red circle, respectively. Because our ejecta masses,  $M_{\text{dyn}}$  and  $M_{\text{wind}}$ , are allowed to reach zero, not all BNSs and NSBHs detected in GWs will have an associated KN. We find that for the fiducial EOS,  $\sim 79\%$  (81%) of our BNS events and  $\sim 12\%$  (14%) of our NSBH events have an associated KN with either  $M_{\text{dyn}}$  or  $M_{\text{wind}} > 10^{-5} M_\odot$  in O4 (O5).

One of the many factors that favor KN detection is a lower total mass of the merging binaries, which is expected, at least for the chosen EOS, as lower-mass stars are typically more easily disrupted. An interesting point to note is that the total

mass appears to be a more significant discriminator between detection/non-detection than the luminosity distance, at least within the O4 and O5 distances probed by our simulations. Moreover, due to its higher sensitivity, *g*-band lets us detect BNS KNe at  $> 720 \text{ Mpc}$ , slightly better than *i*-band, as shown in the top distribution of Figure 4. The 90th percentile of KN detected from BNS merger are expected to have a total mass of  $\lesssim 4.05 M_\odot$  ( $\lesssim 3.95 M_\odot$ ) and are expected to be at a distance  $\lesssim 930 \text{ Mpc}$  ( $\lesssim 830 \text{ Mpc}$ ) in *g*-band (*i*-band).

On the other hand, NSBH KN detections peak at  $\sim 420 \text{ Mpc}$  in *g* band, but for distances  $\gtrsim 600 \text{ Mpc}$ , NSBH KNe are more often detected in *i* band than in *g* band, which is reasonable considering the larger redshifts and the fact that NSBHs can be red due to a small squeezed  $M_{\text{dyn}}$  component and the red wind ejecta component [57]. In fact, the different dynamical ejecta geometry and composition is taken into account in the KN models used: the NSBH KN models do not feature the lanthanide-free polar component assumed for the BNS KNe, thus producing intrinsically redder transients than the BNS KNe [14, 39]. The 90th percentile of the detectable KNe from O5 NSBH mergers is expected to have total mass  $\lesssim 7.02 M_\odot$  ( $\lesssim 8.00 M_\odot$ ) and are expected to be at a distance  $\lesssim 630 \text{ Mpc}$  ( $\lesssim 890 \text{ Mpc}$ ) in *g*-band (*i*-band).

### 2. Mass ratio dependence

In Figure 5, we show the mass ratio and total mass of the BNS and NSBH systems for which GWs are detectable, and the subset for which a KN is also detectable. Although the total mass is a good proxy for KN detection efficiency, the mass ratio also provides a good discriminator. For BNS systems, 76% (81%) of all mergers with  $q < 0.8$  of all KNe and  $\sim 29\%$  ( $\sim 31\%$ ) of all BNS systems detected in GWs are detected in *g* (*i*) bands using our baseline strategy. For more symmetric-mass binaries, the detection efficiency in *g* (*i*) bands falls to 73% (66%) of all KNe and  $\sim 56\%$  ( $\sim 50\%$ ) of all BNS systems detected in GWs. Even though the GW-detected sample favors binaries with near-equal masses (the pairing function is a power law in mass ratio peaking for equal mass binaries), KN detection favors asymmetric mass binaries, where the low mass NS can be more easily disrupted than a higher mass NS.

For NSBH mergers, the mass ratios follow a bimodal distribution, as shown in Figure 5. This is a gravitational wave selection effect, where we interpret the peak at  $q \sim 0.5$  with NSBHs consisting of a BH close to the low-mass edge of the dip in the PDB model. For masses below that edge, there are close to no BHs (although note the transition is smooth in our model), while in the dip, the merger rate decays, hence the peak in the observed mass ratio distribution. Because KN production is favored for low-mass BHs and low-mass NSs, they can only be detected at lower distances. Because of these reasons, the 90th percentile of detectable NSBH KNe lie in a specific region of the mass ratio-distance space ( $q \in [0.2 - 0.6]$  and distance  $< 1 \text{ Gpc}$ ). The rest of the NSBH mass ratio distribution follows from the extension of the BH mass distribution out to masses much larger than the NS mass. KN production is highly suppressed in this regime ( $q < 0.1$ ) since

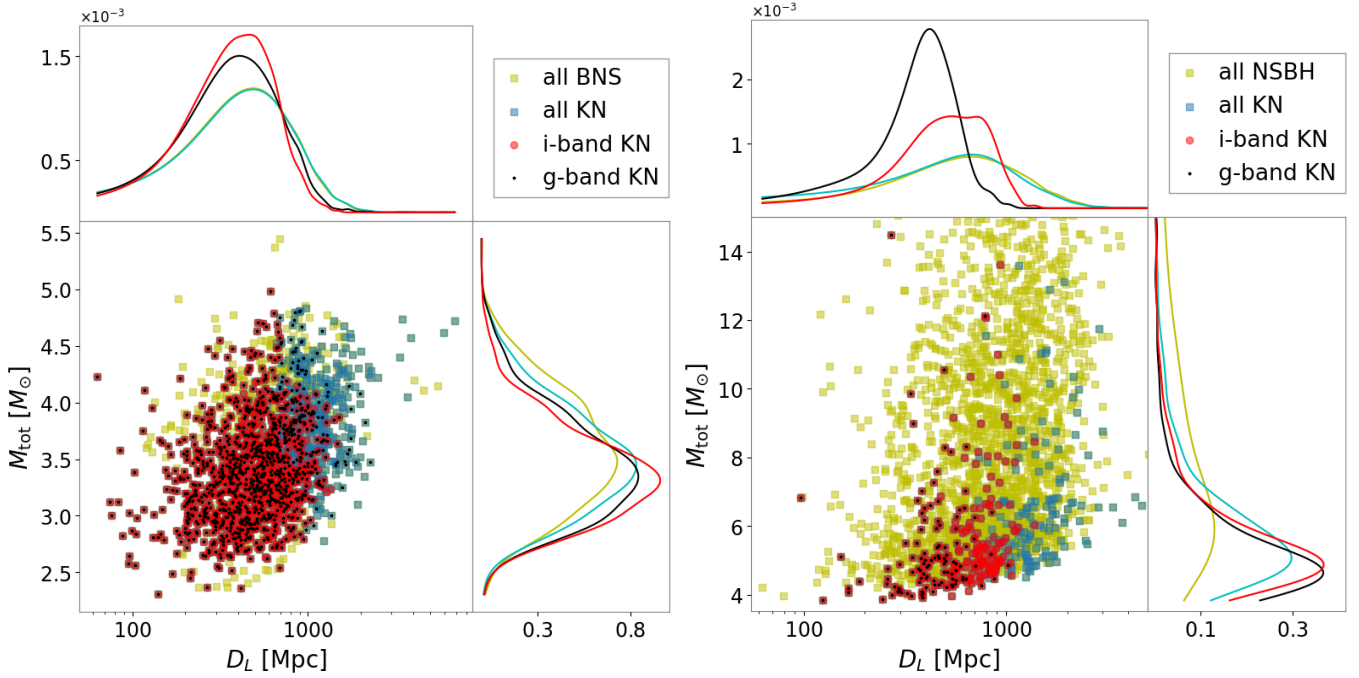


FIG. 4. Total mass versus luminosity distance for BNS (left) and NSBH (right) events in the O5 simulation. The yellow squares represent all BNS/NSBH detected in gravitational waves, the blue squares show all mergers for which a KN is produced according to our model and fiducial EOS. Out of all the KNe, those with a black point and/or a red circle were detected in  $g$  and/or  $i$  band, respectively. The same color scheme applies to the histograms. We limit the plot to  $15 M_{\odot}$  for the NSBH total mass for visualization purposes. For both cases, the lower total mass end of the distribution yields higher KN detection rates than at larger mass.

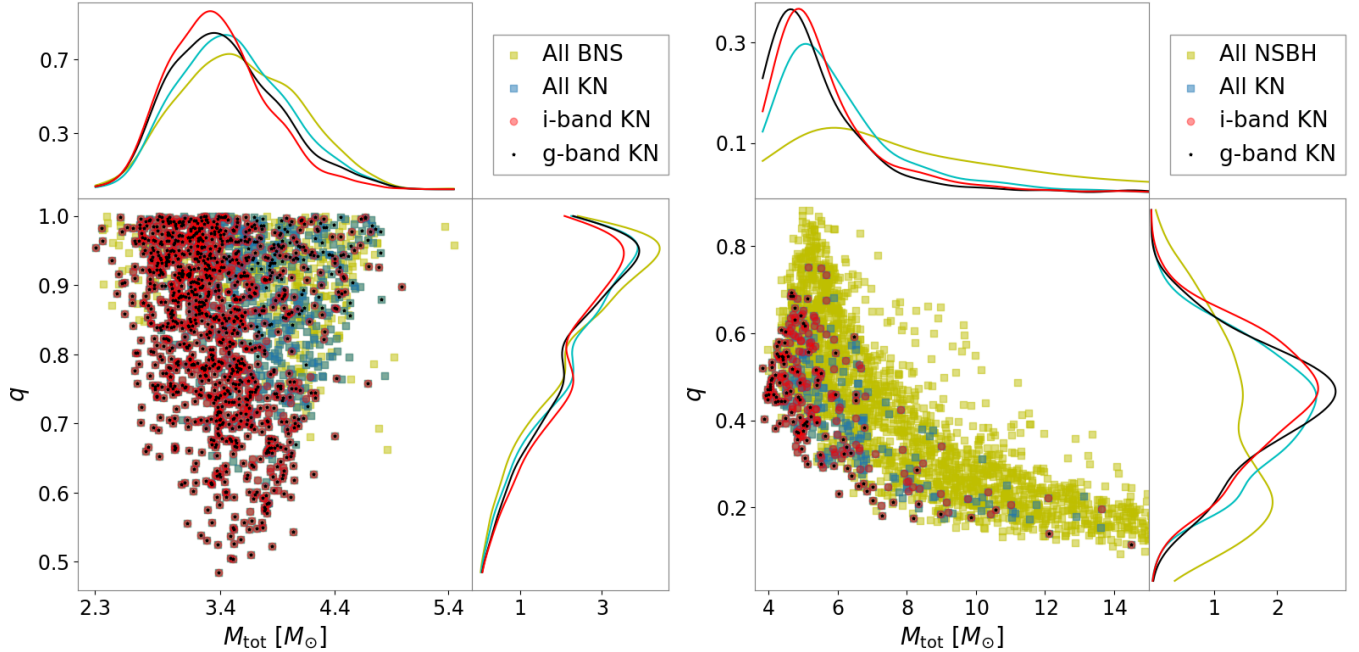


FIG. 5. Mass ratio and total mass for the BNS merger events (left panel) and NSBH mergers (right panel) from the O5 simulation. The color scheme is the same as in Figure 4.

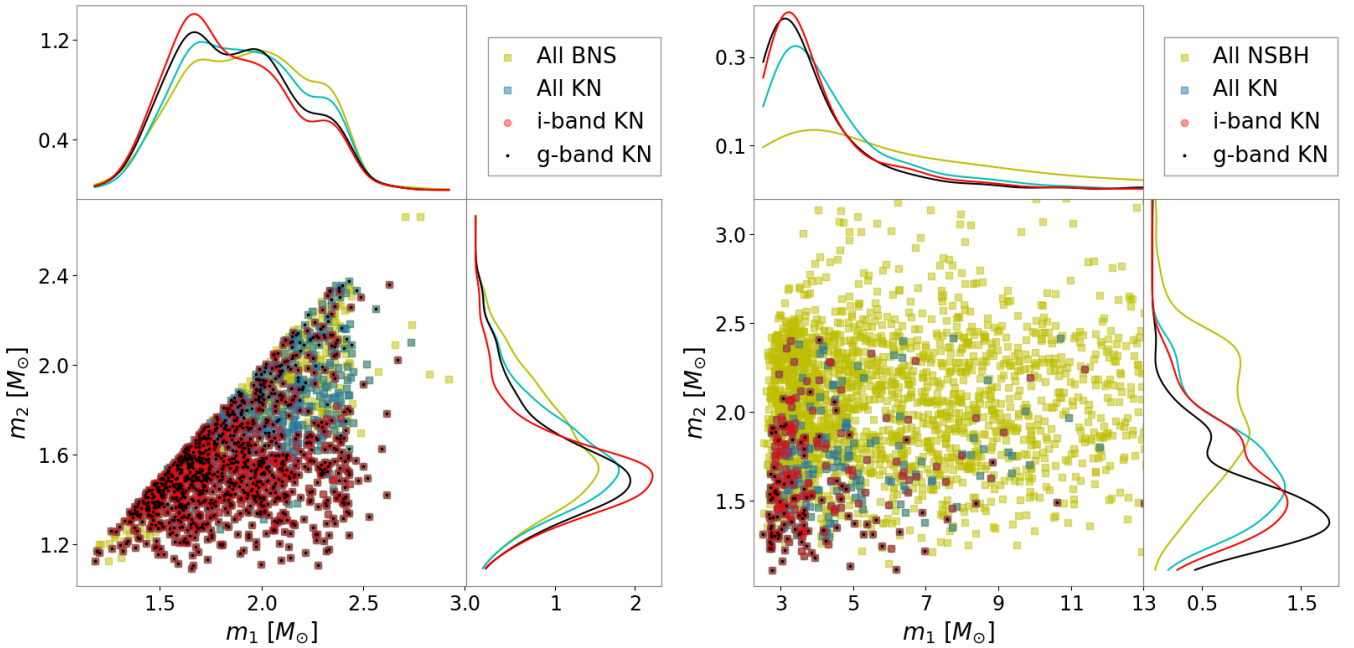


FIG. 6. Component masses of BNS (left) and NSBH (right) systems and their effect on KN detection. We limit  $m_1$  to  $8M_\odot$  in the plot for visualization purposes. The color scheme is the same as in Figure 4.

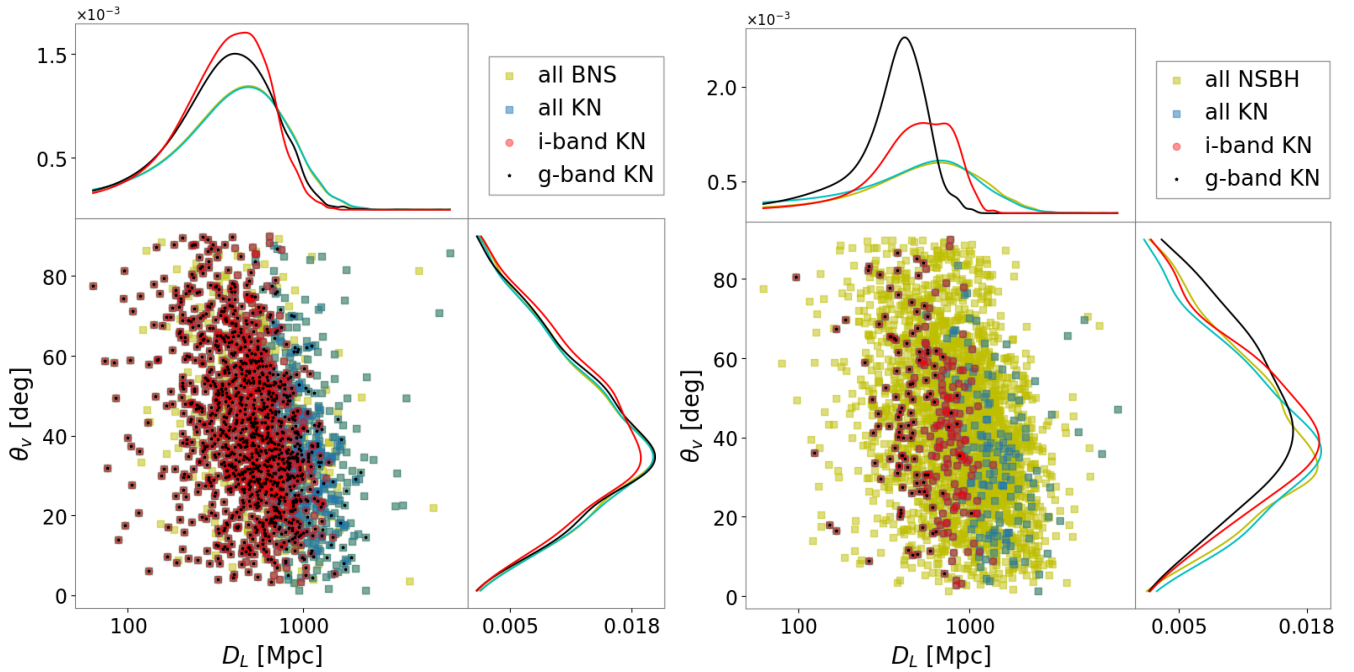


FIG. 7. Viewing angle of the BNS (left) and the NSBH (right) mergers versus their distance for the O5 simulations. The color scheme is the same as in Figure 4.

the highly asymmetric mass ratio would imply that the BH is large enough to engulf the NS before it is tidally disrupted.

### 3. Component mass dependence

Compared to the distribution of GW BNS events, those that result in the detection of a KN clearly shows a preference towards lower values of  $m_2$  as shown in Figure 6.

For BNS mergers, the KN detection efficiency peaks around  $m_1 \sim 1.7 M_\odot$ , with events having  $m_1 \leq 1.7 M_\odot$  detected with an efficiency of 84% (89%) in  $g$  ( $i$ ) band. For  $m_2$ , the detection efficiency peaks at  $1.5 M_\odot$ , where events with  $m_2 \leq 1.5 M_\odot$  are detectable at an efficiency of 91% (95%) in  $g$  ( $i$ ) band respectively. As a result of the increased compactness of the secondary component at higher masses, tidal disruption would not be strong enough to produce significant ejecta mass. The compactness and mass are indeed parameters that explicitly enter in our  $M_{\text{dyn}}$  Eq. 3 prescription, so the existence of a KN detectability dependence on secondary mass is not surprising. The higher sensitivity in  $g$ -band compared to the  $i$ -band makes it easier to detect some of these events in the former, simply because these events tend to be at larger distances than those closer to the peak of the mass distribution (higher mass BNSs have a lower volumetric merger rate than lower mass NSs in our model).

In the NSBH case, the compactness of the NS is also determinant for the launch of ejecta (again, it is explicitly entered in our  $M_{\text{dyn}}$  Eq. 6 and  $M_{\text{wind}}$  Eq. 7 prescriptions). Of course, the BH mass also plays an important role in defining the ISCO radius. The 90th percentile of all NSBH mergers that produce a KN in our simulations have a BH mass  $< 7 M_\odot$ , whereas for NSBH detectable KNe, the 90th percentile BH mass is comparatively smaller with values  $< 6 M_\odot$  in both  $g$  and  $i$  bands. We argue that the reason why we do not have a noticeable  $m_1$  dip around  $3-5 M_\odot$  and subsequent rise at larger BH mass in the GW-detected distribution, although it is present in the astrophysical distribution of BH we assume, is because the pairing function favors near-equal mass binaries, so even if the merger rate of BHs in the dip is lower, the pairing function suppresses NSBH mergers with BHs above the dip.

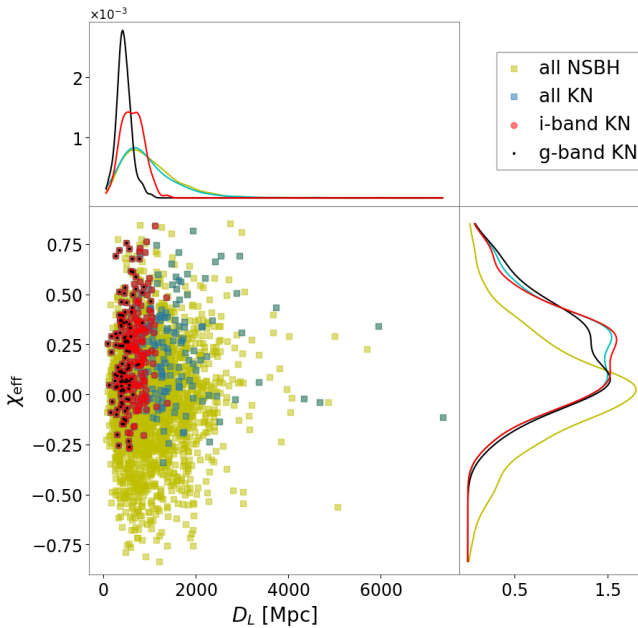


FIG. 8. Effective spin  $\chi_{\text{eff}}$  versus luminosity distance for our O5 simulated NSBH mergers. The color scheme is the same as in Figure 4.

#### 4. Viewing angle dependence

In Figure 7 we show the viewing angle of BNS binaries versus their distance. There is a marginal dependence of KN detectability on viewing angle: systems that are closer to on-axis are seen out to further distances than those more edge-on, with a larger detection in  $g$ -band than in  $i$ -band for objects face-on at larger distances. This is expected as the KNe are typically brighter and bluer along the polar axis.

For what concerns NSBHs, as shown in Figure 7, there does not appear to be an extreme EM selection effect based on viewing angle either. We observe that detectability is primarily driven by the distance of the binary and the composition and geometry of the ejecta. The NSBH KN model we assume includes a planar dynamical component rich in lanthanides, and no squeezed polar dynamical ejecta. Therefore, the dynamical ejecta will typically appear redder than in the BNS case, leading to a larger detectability in  $i$  band than in  $g$  band, especially as we push to larger distances (hence typically less edge-on binaries due to the GW selection effects). To second order, we do observe that detection efficiency is higher for edge-on (e.g. 34-36% in  $g$  and  $i$  for viewing angles  $> 50$  deg below 1 Gpc) than face-on systems (27% in both  $g$  and  $i$  bands for viewing angles  $< 30$  deg below 1 Gpc), due to the geometry of the dynamical ejecta for NSBH KNe.

#### 5. Spin dependence

The spin of the BNS events does not have an impact on KN production and detection as it is not taken into account in our ejecta prescriptions, which is generally justified by the expected small dimensionless spin of the individual stars within BNS systems [110]. Meanwhile, for NSBH mergers, the BH spin has a significant effect on KN production and detection. The radius of the ISCO of a BH is given by:

$$R_{\text{ISCO}} = f(\chi_{\text{BH}}) \frac{GM_{\text{BH}}}{c^2}, \quad (9)$$

where  $6 \leq f(\chi_{\text{BH}}) \leq 9$  for an orbit in which  $\chi_{\text{BH}}$  is anti-aligned with the direction of angular momentum (counter-rotating) and  $1 \leq f(\chi_{\text{BH}}) \leq 6$  when  $\chi_{\text{BH}}$  is aligned with the direction of angular momentum (co-rotating) [19, 95]. For tidal disruption to occur, the disruption radius should be  $r_{\text{disrupt}} \geq R_{\text{ISCO}}$ . This means that tidal disruption is favored for systems with co-rotating BH spins. In Figure 8 we show the dependence of a GW-observable, the effective spin  $\chi_{\text{eff}} = (m_1 \chi_{1z} + m_2 \chi_{2z}) / (m_1 + m_2)$  (where  $\chi_{1z}, \chi_{2z}$  are the components' spins along the binary angular momentum direction), on the detectability of events in our simulations, since the BH spin magnitude, which directly affects the ISCO radius, is typically harder to constrain from GW observations. Because the effective spin is mass-weighted, the BH component has a larger contribution to its value than the NS. We can see that both KN production and detection favor  $-0.2 < \chi_{\text{eff}} < 0.7$ . This is a KN selection effect, not a GW one, as GW selection effects only slightly skew the effective spin distribution [80].

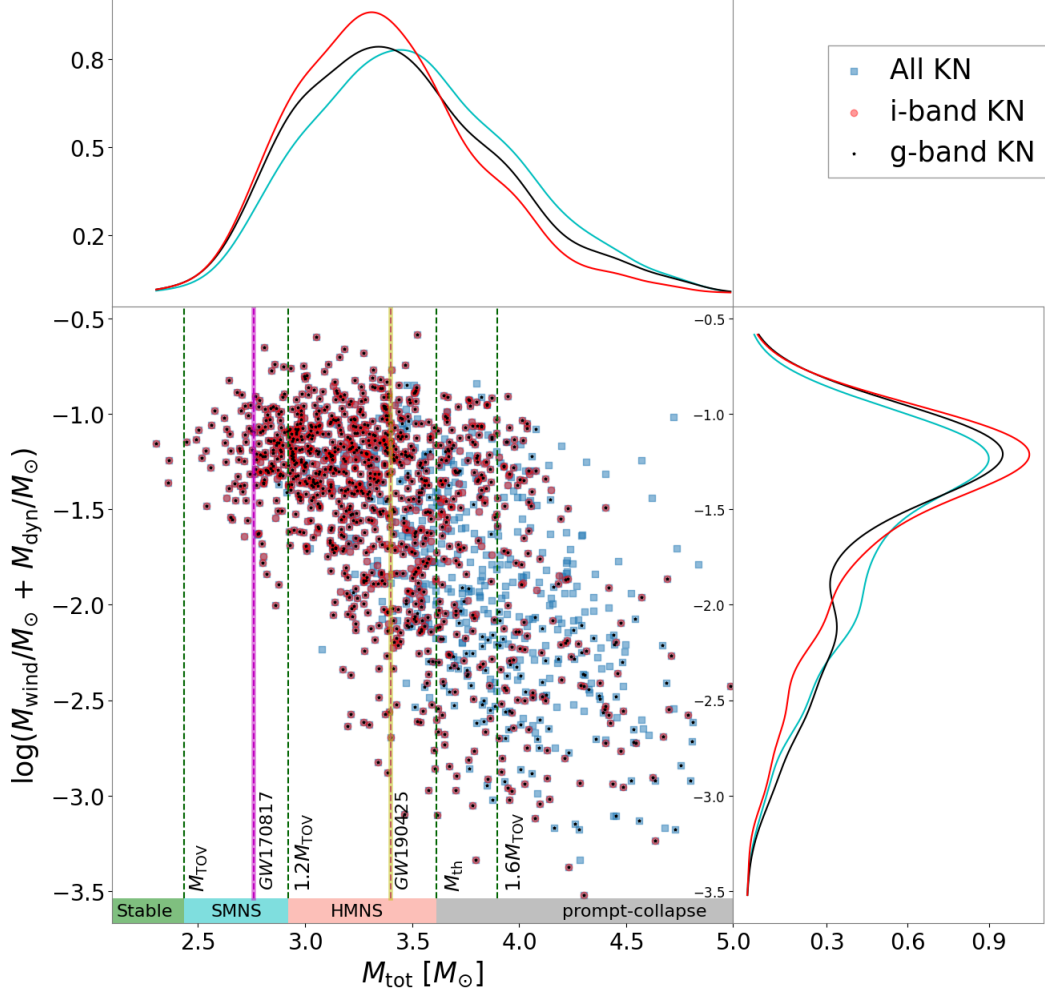


FIG. 9. Total ejected mass from BNS mergers versus their total mass. Vertical dashed lines delineate between different merger remnants fates, with the threshold masses and radii derived assuming the EOS from [54]. Here  $M_{\text{TOV}} = 2.436 M_{\odot}$ ,  $R_{\text{TOV}} = 11.7$  km, and  $M_{\text{th}} = 3.616 M_{\odot}$ . The color scheme is the same as in Figure 4, except that by construction we do not have BNSs that do not produce a KN here. The pink and yellow lines indicate the fate of GW170817 and GW190425 remnants according to our assumptions.

Remnant	Binary mass range	Detectable KNe				BNS GW detections	
		O4		O5		O4	O5
		<i>g</i>	<i>i</i>	<i>g</i>	<i>i</i>		
Stable NS	$M_{\text{tot}} < M_{\text{TOV}}$	$\leq 1\%$	$\leq 1\%$	$\leq 1\%$	$\leq 1\%$	$\leq 1\%$	$\leq 1\%$
SMNS	$M_{\text{TOV}} < M_{\text{tot}} < 1.2 M_{\text{TOV}}$	$\sim 19\%$	$\sim 17\%$	$\sim 12\%$	$\sim 13\%$	$\sim 18\%$	$\sim 9\%$
HMNS	$1.2M_{\text{TOV}} < M_{\text{tot}} < M_{\text{th}}$	$\sim 52\%$	$\sim 53\%$	$\sim 55\%$	$\sim 61\%$	$\sim 51\%$	$\sim 52\%$
Prompt BH	$M_{\text{tot}} > M_{\text{th}}$	$\sim 28\%$	$\sim 29\%$	$\sim 32\%$	$\sim 25\%$	$\sim 30\%$	$\sim 38\%$

TABLE III. Percentage of BNS mergers that falls into each of the remnant categories as predicted by the assumed fiducial EOS in LVK O4 and O5 runs. The “detectable KNe” column shows the fraction of objects with a detectable associated KN for each category, out of all objects with an associated KN. The “BNS GW detections” column refers to the fraction of GW detections falling into each category, out of all GW detections of BNS.

### 6. Fate of the central remnant

The fate of the central remnant and the properties of the ejecta are all related to the masses and spins of the components

of the BNS system [97]. In Figure 9 we show the total (wind and dynamical) ejecta mass in the simulated BNS mergers versus the summed (total) component masses, along with the expected mass ranges for the formation of different kinds of rem-

Run	Binary type	KN detectability	
		g-band	
		(%)	(%)
O4	BNS	96	98
	NSBH	89	99
O5	BNS	74	71
	NSBH	29	64

TABLE IV. KN detection efficiencies (out of the total GW detections with an associated KN production) using our observing strategy for a fiducial depth of  $g = 24.3$  and  $i = 23.9$  and the fiducial EOS. Here O4 refers to simulation 2

nant. A hypermassive NS (HMNS) is a massive NS remnant, supported mainly by its differential rotation, that will collapse to a BH within tens to hundreds of milliseconds following the merger as mass accretion continues [98]. A supramassive NS (SMNS) is a less massive NS supported by its solid body rotation and can survive a few hundreds of milliseconds until the remnant spin downs to a point of collapse [75]. Above the threshold mass, we expect prompt collapse to a black hole. Note that GW170817-like events result in a SMNS remnant using our fiducial EOS, whereas with our softer EOS, such events are expected to produce a HMNS remnant. Previous work on GW170817 [47] excludes the possibility of a long-lived stable NS remnant, since a BH is most likely required [92] to facilitate a relativistic outflow that would power a short GRB, but they could not exclude the possibility of a SMNS remnant with a magnetar-like surface dipole magnetic field powering a GRB [46, 76, 108] before it would ultimately collapse into a BH. Other works [88] mention the possibility of a remnant SMNS if  $M_{\text{TOV}} \geq 2.16 M_{\odot}$ , which corresponds to the case of the fiducial EOS used in this work ( $M_{\text{TOV}} = 2.436 M_{\odot}$ ). The possibility of a SMNS remnant is also explored by [71] whose work points to GW170817 producing either a HMNS or a short-lived SMNS.

The threshold mass  $M_{\text{th}}$  depends primarily on the EOS used [21, 51], but also on mass ratio. Symmetric mass ratio systems have higher  $M_{\text{th}}$  (by  $\sim 0.1 - 0.3 M_{\odot}$  for a mass ratio of 0.6) compared to asymmetric-mass BNS systems. This follows from the fact that symmetric-mass binary systems have higher angular momentum at a given orbital separation compared to more asymmetric binaries assuming the same  $M_{\text{tot}}$  [22], which facilitates stabilization of the remnant against collapse. For our fiducial EOS,  $M_{\text{th}}$  takes a value of  $3.62 M_{\odot}$ , and we ignore the effect of mass ratio since our pairing function strongly disfavors asymmetric BNSs with  $q < 0.5$ .

As shown in Table III, most BNS we will detect in GWs are likely to result in an HMNS, but a noticeable fraction of multimessenger sources will promptly collapse into a BH. The ejected mass of multimessenger sources peaks around  $10^{-1.23} M_{\odot}$ . In our simulation,  $\sim 1\%$  of both the BNS KN detections and the GW detections arise from a system that likely results in stable NS remnants, while we expect at least 17% of the O4 detections to be from sources that would likely produce SMNS and at least 52% from sources that result in

HMNS remnants. This number comes to about 12% in O5 for SMNS and 55-61% for HMNS remnants. Around 29% of the KN detections in the O4 simulations and 32% of KN detections from the O5 simulations are from sources that would undergo a prompt collapse. Although the finding that most BNS mergers will produce an HMNS is in agreement with [72], they find that a negligible fraction of objects will undergo prompt collapse. This is a result of the different mass distributions assumed, as [72] uses a narrow symmetric mass distribution motivated by Galactic binaries. Such distribution is significantly lighter than the one used in this work, which accommodates for events such as GW190425 [5], not easily explained by the Galactic binary population.

It is worth noting that, at least in our GW population, the volumetric merger rate of compact objects in the NS mass regime decreases with mass. Hence, the most massive systems are rarer than lower-mass objects. For this reason, and because of the larger volume probed by the O5 network, a larger fraction of GW detections are expected to promptly collapse in a BH in O5 compared to O4, which diminishes the fraction of objects producing a SMNS or an HMNS (see the last columns of Table III).

### C. Sky tiling and overall detection rate

For each simulated event, we use `gwemopt` to produce an observing plan, which determines whether our default observing strategy would cover the true location of the merger. Combined with the detectability results from the previous subsection, this provides an estimate of the percentage of events that may have a KN detected in the O4 and O5 observing runs.

For example, Figure 10 shows the DECam tilings for an example BNS event from simulation 2 at 174 Mpc localized to 37 sq. deg. at 90% CI. In O4, only 3% of the BNS events are expected to be so well-localized. We find that DECam is able to cover the 90% probability region for this well-localized event almost entirely with only  $\sim 17$  pointings. Our baseline case assumes the follow up is performed 1 day after the GW trigger.

The results shown above only assume a single value of the depth for all events. The KN detection efficiency out of the total GW detection with an associated KN production is shown in Table IV. In reality, we want to adjust the depth (and filters) based on the Moon phase and findings of this work for the KN population at different distances. For this reason, we provide the quantiles of our KN population at different distances and times in Table V for BNS events and VI for NSBH events, so that these can be used to inform the depth of follow-up campaigns with DECam and other instruments.

For our case, we run `gwemopt` assuming these different depths of up to 24.3 and 23.9 in  $g$  and  $i$ , respectively, and a maximum on-sky time of 4 hours. With these optimized settings, in O4 (O5), we expect to cover about 30% (38%) of all BNS KNe within 1 day of explosion and 28% (30%) of NSBH KNe within 2 days of explosion. Table VII summarizes the detection efficiency with `gwemopt` in  $g$  and  $i$  bands for all scenarios. These percentages now reflect both the fact that the

Distance (Mpc)	Observing run	band	mag <sub>50</sub>					mag <sub>70</sub>					mag <sub>90</sub>							
			12h	1d	2d	3d	4d	5d	12h	1d	2d	3d	4d	5d	12h	1d	2d	3d	4d	5d
< 100	O4	<i>g</i>	19.0	18.4	19.5	21.0	22.3	23.2	19.7	19.1	20.3	21.6	22.9	23.9	20.2	20.3	21.4	22.6	23.6	24.5
		<i>i</i>	19.0	18.2	19.3	20.2	21.0	21.7	19.4	18.6	19.6	20.7	21.6	22.3	20.0	19.3	19.9	21.1	21.9	22.7
	O5	<i>g</i>	19.8	19.8	20.1	21.1	22.0	22.8	20.1	20.1	20.8	21.9	22.5	23.2	20.2	20.3	21.4	22.8	23.9	24.9
		<i>i</i>	19.5	18.7	19.1	19.7	20.3	20.8	20.0	19.3	19.6	20.7	21.6	22.4	20.3	19.6	19.9	21.1	22.1	22.9
100-150	O4	<i>g</i>	20.3	19.8	20.7	22.1	23.3	24.2	20.8	20.5	21.4	22.7	23.9	24.8	21.2	21.2	21.8	23.2	24.4	25.4
		<i>i</i>	20.5	19.7	20.4	21.2	22.0	22.7	20.7	20.0	20.8	21.8	22.6	23.3	21.2	20.6	21.0	22.3	23.2	23.9
	O5	<i>g</i>	19.8	19.1	19.9	21.3	22.6	23.6	20.1	19.5	20.3	21.7	23.1	23.8	20.6	20.4	21.7	22.7	23.6	24.5
		<i>i</i>	20.3	19.5	20.3	21.0	21.6	22.3	20.5	19.6	20.4	21.5	22.4	23.1	20.8	20.4	20.7	21.8	22.7	23.4
150-200	O4	<i>g</i>	20.7	20.1	21.1	22.4	23.7	24.7	21.2	20.7	21.6	23.0	24.3	25.3	21.7	21.4	22.2	23.5	24.9	25.9
		<i>i</i>	20.9	20.1	21.1	22.0	22.8	23.5	21.2	20.3	21.3	22.6	23.4	24.2	21.5	20.8	21.6	22.9	23.8	24.6
	O5	<i>g</i>	21.0	20.3	21.4	22.7	24.1	25.0	21.2	20.9	22.0	23.4	24.6	25.6	21.9	21.8	23.0	24.2	25.0	25.8
		<i>i</i>	21.1	20.3	21.3	22.2	23.0	23.8	21.3	20.5	21.4	22.6	23.5	24.2	21.8	21.4	21.6	22.8	23.7	24.4
200-250	O4	<i>g</i>	21.4	20.7	21.6	23.0	24.2	25.1	21.6	21.1	22.1	23.4	24.7	25.7	22.1	21.8	22.8	24.2	25.3	26.3
		<i>i</i>	21.5	20.7	21.4	22.2	23.1	23.8	21.7	20.8	21.7	23.0	23.9	24.6	22.0	21.3	22.1	23.3	24.2	25.0
	O5	<i>g</i>	21.6	21.0	21.9	23.1	24.4	25.1	21.8	21.6	22.5	23.7	24.7	25.7	22.2	22.2	23.0	24.4	25.4	26.3
		<i>i</i>	21.7	20.9	21.3	21.9	22.6	23.2	21.9	21.2	21.6	22.5	23.3	24.0	22.5	22.0	22.0	23.2	24.1	24.8
250-300	O4	<i>g</i>	21.8	21.0	22.0	23.4	24.6	25.5	22.0	21.5	22.4	23.9	25.2	26.3	22.4	22.0	23.1	24.5	25.7	26.8
		<i>i</i>	21.9	21.0	21.7	22.6	23.4	24.0	22.1	21.3	22.2	23.4	24.3	25.0	22.5	21.7	22.4	23.7	24.7	25.4
	O5	<i>g</i>	21.9	21.3	22.2	23.4	24.6	25.5	22.3	21.8	22.6	24.0	25.2	26.1	22.5	22.4	23.2	24.5	25.7	26.7
		<i>i</i>	22.1	21.2	21.8	22.5	23.2	23.8	22.3	21.7	22.2	23.2	24.1	24.8	22.7	22.2	22.4	23.6	24.5	25.3
300-500	O4	<i>g</i>	22.5	21.7	22.5	23.9	25.1	26.1	22.8	22.1	23.0	24.4	25.7	26.7	23.3	22.9	23.8	25.1	26.4	27.4
		<i>i</i>	22.6	21.7	22.4	23.3	24.1	24.8	22.8	22.0	22.7	23.9	24.8	25.5	23.2	22.4	23.2	24.4	25.3	26.0
	O5	<i>g</i>	22.7	21.9	22.8	24.2	25.3	26.2	23.0	22.5	23.4	24.7	25.8	26.8	23.6	23.3	24.0	25.3	26.5	27.5
		<i>i</i>	22.9	22.0	22.5	23.3	24.0	24.7	23.2	22.3	22.9	23.9	24.8	25.5	23.6	22.9	23.3	24.5	25.5	26.2

TABLE V. 50th, 70th, and 90th quantiles of the KN magnitude distributions at 0.5,1,2,3,4 and 5 days for the BNS mergers at O4 and O5 sensitivities.

location of the KN is observable and covered by the scheduler and that the KN luminosity was above the flux limit. Considering the observability constraints that we place on airmass and moon distance, it is reasonable that about  $\sim 38\%$  of KNe from BNS events are covered by our DECam scheduler in O5. NSBH KNe result in a lower coverage probability because the depths needed to detect the EM counterpart are significantly larger, hence the longer exposure times required resulting in smaller sky areas being covered in the fixed time window, despite the GW localizations of BNS and NSBH mergers appearing similar in our simulations.

Next, we compute how many events we expect to detect in GW and also jointly with a KN, based on the GW detection rates and our KN detection efficiency. For DECam-like instruments, we estimate BNS (NSBH) KN detectability rate of  $1-16 \text{ yr}^{-1}$  ( $0-1 \text{ yr}^{-1}$ ) in O4 and  $16-165 \text{ yr}^{-1}$  ( $1-12 \text{ yr}^{-1}$ ) in O5 respectively. These ranges take into account the uncertainty on the latest rate estimates and on the EOS, with the rates contributing the most to the final uncertainty. These rates drop if corrected for our `gwemopt` observability efficiency, which can be calculated from Tables IX and X in Appendix A as  $\sim 0-5 \text{ yr}^{-1}$  ( $0 \text{ yr}^{-1}$ ) and  $\sim 6-66 \text{ yr}^{-1}$  ( $\sim 0-3 \text{ yr}^{-1}$ )

multimessenger BNS (NSBH) detections in O4 and O5. If we consider the non-detection of BNS mergers in O4 up until the end of 2024 (see Table VIII), the BNS KN detectability rate drops to  $0-7 \text{ yr}^{-1}$  in O4 and  $7-74 \text{ yr}^{-1}$  in O5; when corrected for our `gwemopt` observability efficiency, the rate drops to  $0-2 \text{ yr}^{-1}$  in O4 and  $2-28 \text{ yr}^{-1}$  in O5.

We note that even though the O4 GW BNS merger rates we find may appear large given the non-detection of high-confidence BNS candidates in O4, our detection rate (as also in other works such as [60]) is based on an SNR cut that does not correspond exactly to the O4 search pipelines selection criteria, based on False Alarm Rate (FAR) instead. Therefore, our selection may include events that would be considered sub-threshold in the actual O4 searches. However, the expected number of multimessenger sources is likely to be closer to what we will actually find in O4, modulo the uncertain rates that may push us towards the lower limits we report, given that those sources are typically the better localized and more nearby, and will have the largest SNR and lower FAR of the entire BNS population. In our simulations release, we include detector and network SNRs, so our findings can easily be rescaled in light of the new findings from the O4 search

Distance	Observing run	band	mag <sub>50</sub>					mag <sub>70</sub>					mag <sub>90</sub>							
			12h	1d	2d	3d	4d	5d	12h	1d	2d	3d	4d	5d	12h	1d	2d	3d	4d	5d
< 200	O4	<i>g</i>	22.6	21.6	21.6	21.9	22.8	23.6	22.8	21.8	21.9	22.4	23.2	24.1	23.1	22.2	22.2	22.7	23.6	24.4
		<i>i</i>	20.7	20.1	20.0	20.4	20.9	21.4	21.1	20.5	20.5	20.9	21.3	21.8	21.9	21.1	21.0	21.2	21.7	22.3
	O5	<i>g</i>	22.3	21.4	21.4	21.8	22.6	23.5	22.5	21.6	21.6	22.1	22.7	23.6	22.6	21.7	21.8	22.4	23.1	23.8
		<i>i</i>	20.6	19.9	19.9	20.2	20.5	21.0	20.8	20.1	20.0	20.3	20.6	21.2	21.1	20.5	20.4	20.5	20.9	21.4
200-300	O4	<i>g</i>	23.6	22.5	22.6	23.1	23.8	24.6	23.8	22.7	22.8	23.2	23.9	24.7	24.0	22.9	23.0	23.6	24.3	25.1
		<i>i</i>	21.7	21.3	21.1	21.4	21.8	22.2	22.0	21.4	21.4	21.7	22.1	22.6	22.3	21.7	21.6	22.1	22.5	23.2
	O5	<i>g</i>	24.0	22.9	23.0	23.5	24.2	25.0	24.0	23.0	23.1	23.6	24.4	25.3	24.3	23.3	23.3	23.9	24.7	25.5
		<i>i</i>	22.1	21.4	21.4	21.8	22.1	22.6	22.3	21.6	21.5	21.8	22.2	22.7	23.4	22.5	22.4	22.8	23.4	23.4
300-400	O4	<i>g</i>	24.2	23.0	23.1	23.6	24.3	25.0	24.3	23.2	23.3	23.8	24.4	25.1	24.5	23.3	23.4	23.9	24.6	25.4
		<i>i</i>	22.4	21.7	21.7	22.0	22.4	22.8	22.7	21.9	21.8	22.3	22.8	23.3	22.9	22.2	22.2	22.5	23.0	23.5
	O5	<i>g</i>	24.5	23.5	23.5	24.0	24.7	25.5	24.7	23.5	23.6	24.1	24.9	25.6	25.0	23.9	23.8	24.3	25.1	26.0
		<i>i</i>	22.8	22.1	22.0	22.4	22.8	23.3	23.0	22.6	22.5	22.7	23.2	23.8	23.7	23.0	22.9	23.3	23.8	24.3
400-500	O4	<i>g</i>	25.0	23.8	24.0	24.5	25.1	25.8	25.1	24.0	24.1	24.6	25.2	26.0	25.4	24.0	24.1	24.6	25.3	26.1
		<i>i</i>	23.0	22.4	22.3	22.6	23.0	23.4	23.1	22.5	22.4	22.8	23.1	23.6	23.2	22.8	22.8	23.2	23.6	24.2
	O5	<i>g</i>	24.8	23.8	23.8	24.2	24.9	25.6	25.1	23.9	24.0	24.4	25.1	25.9	25.3	24.0	24.1	24.6	25.3	26.0
		<i>i</i>	23.0	22.4	22.3	22.6	23.0	23.4	23.2	22.5	22.4	23.0	23.4	23.8	23.6	22.9	22.9	23.2	23.8	24.4
500-600	O4	<i>g</i>	25.4	24.2	24.2	24.6	25.2	25.9	25.6	24.3	24.3	24.8	25.4	26.1	25.8	24.4	24.5	25.0	25.7	26.5
		<i>i</i>	23.5	23.0	22.9	23.2	23.4	23.8	23.7	23.3	23.2	23.5	24.0	24.6	24.3	23.4	23.4	23.8	24.3	25.0
	O5	<i>g</i>	25.4	24.3	24.3	24.8	25.4	26.1	25.5	24.3	24.4	24.9	25.6	26.4	25.7	24.5	24.5	25.0	25.7	26.5
		<i>i</i>	23.5	22.8	22.8	23.1	23.4	23.8	23.8	23.1	23.0	23.3	23.7	24.3	24.3	23.4	23.4	23.7	24.1	24.7
600-700	O4	<i>g</i>	25.5	24.4	24.4	24.9	25.5	26.2	25.7	24.4	24.6	25.1	25.8	26.5	25.9	24.6	24.7	25.2	25.9	26.6
		<i>i</i>	23.6	23.0	22.9	23.3	23.7	24.2	23.7	23.2	23.1	23.6	23.9	24.4	24.1	23.3	23.3	23.7	24.2	24.8
	O5	<i>g</i>	25.6	24.4	24.5	24.9	25.5	26.1	25.6	24.5	24.6	25.0	25.6	26.3	25.8	24.7	24.6	25.1	25.8	26.6
		<i>i</i>	23.8	23.1	23.0	23.3	23.5	23.9	24.1	23.3	23.2	23.4	23.7	24.3	24.4	23.5	23.4	23.8	24.3	25.0

TABLE VI. 50th, 70th, and 90th quantiles of the KN magnitude distributions at 0.5,1,2,3,4 and 5 days for the NSBH mergers at O4 and O5 sensitivities.

Run	Binary type	gwemopt coverage		KN detectability		
				<i>g</i> -band	<i>i</i> -band	(%)
O4	BNS	30		100		96
	NSBH	28		100		100
O5	BNS	38		99		80
	NSBH	30		60		97

TABLE VII. Detection efficiencies using gwemopt for different scenarios assuming the fiducial EOS and our fiducial observing strategy. The KN detectability columns shows the percentage of kilonovae covered by gwemopt that is detectable in *g* or *i*-band given our fiducial depth. Results for the softer and stiffer EOSs are shown in Appendix A.

pipelines and the relation between their FARs and SNRs, as well as in light of updated rates.

Lastly, we point to the fact that different EOS will predict slightly different KN emission and therefore detection rates

(e.g. [36, 93, 109]). We find that the detection rate is only mildly dependent on the EOS, so that the uncertainty on our detection rate is dominated by the underlying compact object volumetric merger rate uncertainty rather than by changes in the EOS.

#### IV. DISCUSSION

Although we have assumed the same relations to map BNS properties into ejecta masses regardless of the fate of the central remnant, some differences may be expected for different remnants [59], especially when a stable NS is formed. The major difference is expected to be in the wind/outflows mass ejecta rather than in the dynamical ejecta. However, this accounts for < 1% of all BNS systems considered in both O4 and O5, and it is therefore only expected to be a minor perturbation for our results.

Next, we compare our work with previous efforts on GW localizations and KN detectability. Compared to [55] we consider more up-to-date detector sensitivities and simulate

Run	Binary type	GW detection rate	KN detectability	
			<i>g</i> -band (yr <sup>-1</sup> )	<i>i</i> -band (yr <sup>-1</sup> )
O4	BNS	1.0 - 8.6	0.67 - 7.1	0.69 - 7.1
	NSBH	1.6 - 9.1	0.14 - 1.05	0.15 - 1.2
O5	BNS	13 - 110	7.4 - 74	6.6 - 72
	NSBH	18 - 110	0.7 - 5.5	1.4 - 11.0

TABLE VIII. Expected BNS and NSBH detection rates from our LVK O4 and O5 simulations and the associated multimessenger KN detection rates in *g* and *i* bands, assuming different EOSs. The BNS rate calculation assumes that there were no BNS detections in O4 until the end of 2024.

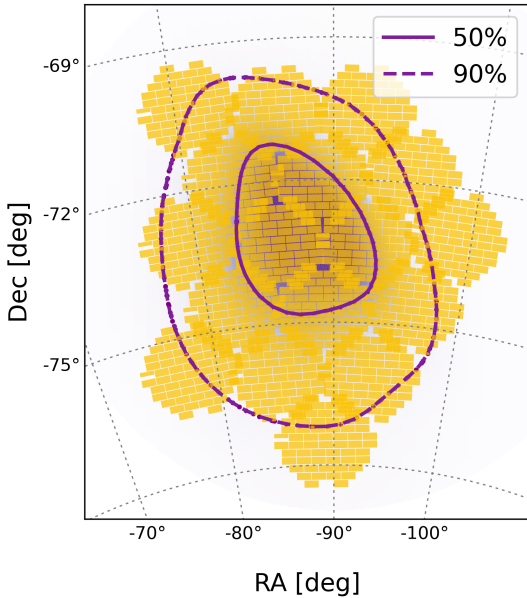


FIG. 10. Simulated DECam tiling follow-up of a well-localized BNS event. The solid and dashed lines indicate the 50 and 90% CI area of the event, respectively. It can be seen that the 90% probability region of the event is covered almost entirely by DECam with  $\sim 15$  pointings.

KN lightcurves. The main differences from the studies in [33, 34, 96] are that we assume a mass distribution driven by GW observations and provide the depth needed to detect a significant fraction of BNS and NSBH KN. In [60] the aim is to understand how multimessenger observations will help in estimating the Hubble constant and focused on the Zwicky Transient Facility (ZTF) for the optimization. We also add to the work presented in [27], which focuses on DECam follow up in O4, by using more updated gravitational wave simulations, physically motivated KN light curves, as well as the addition of O5.

[25] also explore multimessenger prospects for NSBH mergers based on the findings from GWTC-3. A major difference from that work is that they impose an empty lower mass gap, while we allow it to be populated with mass gap NSBHs, which is reasonable based on the detection of GW230529 [1].

This is expected to produce a larger number of NSBHs giving rise to an EM counterpart in our work. On the other hand, given the lack of NSBH detections with BH mass  $> 20 M_{\odot}$ , their population of NSBH binaries has a BH mass cut off at  $> 20 M_{\odot}$ . Because the GW population assumed in our analysis does not distinguish between compact object binary types and can therefore include higher mass BHs following [41], our BH cutoff is effectively at  $60 M_{\odot}$  for NSBH binaries. Although this choice may reduce the fractional number of multimessenger NSBH sources compared to a lower BH mass cut-off, the pairing function would rarely allow for the presence of extreme mass ratio pairings between a  $> 20 M_{\odot}$  BH and a NS (it can be seen from Figure 6 that  $m_1$  in our NSBH population has already tailed off at  $13 M_{\odot}$ ). In our simulations, as we go from softer to stiffer EOS, we find that  $\sim 9 - 14\%$  of NSBHs in O4 are expected to produce a KN of which  $0.4_{-0.2}^{+0.4} - 0.6_{-0.4}^{+0.7}$  per year would be detectable in O4 given our fiducial depth. In O5, we find that  $\sim 11 - 18\%$  of NSBH events are expected to produce a KN depending on the EOS and  $1.9_{-1.2}^{+2.3} - 5.4_{-3.4}^{+6.3}$  per year would be detectable given our fiducial depth. As a result, our prospects for detecting multimessenger NSBH events are promising.

Our findings reveal strong dependencies of KN detection efficiency on the binaries mass (and spin for NSBHs) parameters. This is not surprising as our mapping between binary parameters and ejecta mass explicitly includes these quantities. However, this also indicates that a significant EM selection function will be at play and should be taken into account when multimessenger studies of populations of BNSs and NSBHs, such as EOS and standard siren measurements, will become possible.

To conclude, if masses were to be released in public GW alerts, this would be an invaluable tool for the astronomical community to further inform their follow-up [72] and, for example, prioritize low-mass binaries in place of more massive systems. A caveat is that we have considered detecting any KN that is brighter in at least one band than the magnitude limit considered in our baseline observing strategy. In reality, one would typically require at least two detections of the transient in order to discriminate between moving objects (a major contaminant in transient searches) and static variables, while also identifying transients that most resemble the colors and evolution of a KN. Various tools and methods can be used to rapidly identify them, even with a few data points (e.g., [82]).

## V. CONCLUSIONS

In this work, we describe an end-to-end simulation of GW merger events for the fourth and fifth LIGO/Virgo/KAGRA observing runs to optimize follow-up strategies with our GW-MMADS DECam Survey program. We focus on mergers containing at least one neutron star. We study both the BNS and NSBH parameters and their effect on kilonova production and detectability, finally optimizing our observing strategy based on the expected KN population. The implications of this simulation study can be summarized as follows:

- (i) Including Virgo, even at O3 sensitivity, in the O4 detector network results in larger detection rates of well-localized events at distances  $< 100$  Mpc. Approximately 15% of the BNS and NSBH events are likely to result in a localization that is  $< 500$  sq. deg. in O4, which in O5, increases to 26–28%. More than 10% of the neutron star merger events will have an area which is  $< 100$  sq deg in O5.
- (ii) For our baseline strategy (without considering the gwemopt coverage), we find that in O5, out of all GW detections, KNe are detectable for  $\sim 60\%$  (58%) of BNS mergers and  $\sim 4\%$  (9%) NSBH mergers, at a depth of 24.3 and 23.9 mag in  $g$  and  $i$  respectively. These depths can be optimized for a specific follow-up given an event’s distance; we provide tables with quantiles of the magnitudes for our expected KN population to allow for that.
- (iii) The majority of BNS sources detected in GWs as well as those that have a KN detection are expected to produce a HMNS remnant, while a significant fraction of the remaining detections are likely to undergo prompt collapse to a BH.
- (iv) We show the dependence of KN detectability on GW parameters, providing a realistic population of GW detections. In particular, we show the importance of releasing even tentative chirp masses and mass ratios to the EM follow-up community to inform their triggering criteria and follow-up strategy. The multimessenger BNS detection rate is highest for masses  $M_{\text{tot}} < 4 M_{\odot}$ , peaking around  $M_{\text{tot}} \sim 3.4 M_{\odot}$ . The detection efficiency is also higher for mass ratios  $< 0.8$  compared to more symmetric BNSs. For NSBH mergers, detectability is highest at  $M_{\text{tot}} < 7 M_{\odot}$ , mass ratios of  $\sim 0.5$ , and effective spin  $-0.2 < \chi_{\text{eff}} < 0.7$ , i.e., strongly favoring co-aligned BH spins with respect to the angular momentum of the binary.
- (vi) For DECam-like instruments, considering the non-detection of BNS mergers in O4 up until the end of 2024, we estimate a KN detectability rate of  $\sim 0-7 \text{ yr}^{-1}$  from BNS mergers and  $0-1 \text{ yr}^{-1}$  from NSBH mergers in O4. In O5, our estimated KN detectability rate is  $\sim 7-74 \text{ yr}^{-1}$  from BNS mergers and  $\sim 1-11 \text{ yr}^{-1}$  from NSBH mergers. Taking into account our typical gwemopt coverage, this leads to  $\sim 0-2$  ( $\sim 2-28$ )  $\text{yr}^{-1}$  multimessenger BNS detection and probably no ( $\sim 0-3 \text{ yr}^{-1}$ ) NSBH detection in O4 (O5). Our expectation is that there is a significant probability of detecting an EM counterpart to an NSBH merger in O5.

## ACKNOWLEDGEMENTS

Antonella Palmese acknowledges support for this work by NSF Grant No. 2308193. Mattia Bulla acknowledges the Department of Physics and Earth Science of the University of Ferrara for the financial support through the FIRD 2024 grant. Tim Dietrich acknowledges funding from the European Union (ERC, SMArt, 101076369). Views and opinions expressed are those of the authors only and do not necessarily reflect those of the European Union or the European Research Council. Neither the European Union nor the granting authority can be held responsible for them. Brendan O’Connor is supported by the McWilliams Postdoctoral Fellowship at Carnegie Mellon University. This research used resources of the National Energy Research Scientific Computing Center, a DOE Office of Science User Facility supported by the Office of Science of the U.S. Department of Energy under Contract No. DE-AC02-05CH11231 using NERSC award HEP-ERCAP0029208 and HEP-ERCAP0022871. This work used resources on the Vera Cluster at the Pittsburgh Supercomputing Center. We thank T.J. Olesky and the PSC staff for help with setting up our software on the Vera Cluster.

## Appendix A: Detection efficiency estimate

We calculate the gwemopt coverage and the associated KN detectability for the simulated events also assuming our softer and stiffer EOSs. The results are shown below in Table IX and Table X.

Run	Binary type	gwemopt coverage (%)	KN detectability	
			<i>g</i> -band (%)	<i>i</i> -band (%)
O4	BNS	30	100	89
	NSBH	27	100	100
O5	BNS	39	99	87
	NSBH	28	69	95

TABLE IX. Detection efficiencies using our observing strategy for different scenarios and binaries using the softer EOS.

Run	Binary type	gwemopt coverage (%)	Detectability	
			<i>g</i> -band (%)	<i>i</i> -band (%)
O4	BNS	32	100	99
	NSBH	31	100	100
O5	BNS	39	98	92
	NSBH	31	71	100

TABLE X. Detection efficiencies using our observing strategy for different scenarios and binaries using the stiffer EOS.

We also calculate the KN detectability range from softer to stiffer EOSs, taking into account the non-detection of BNS mergers in O4a. The results are shown below in Table XI. We note that these values differs from what is provided in Table VIII, as only the non-detection of BNS mergers in O4a (thus without including O4b until the end of 2024) is assumed here. We provide this in alternative to our fiducial result, in case the reader prefers to only account for O4a.

Run	Binary type	GW detection rate	KN detectability	
			<i>g</i> -band (yr <sup>-1</sup> )	<i>i</i> -band (yr <sup>-1</sup> )
O4	BNS	1.3 - 11.0	0.8 - 9.1	0.9 - 9.2
O5	BNS	16 - 140	8.9 - 91	8.1 - 88

TABLE XI. Expected BNS detection rates from our LVK O4 and O5 simulations and the associated multimessenger KN detection rates in *g* and *i* bands, the KN detectability range is from softer to stiffer EOSs taking into account the non-detection of BNS mergers during O4a.

---

[1] Abac, A. G., et al. 2024, *The Astrophysical Journal Letters*, **970**, L34

[2] Abbott, B. P., Abbott, R., Abbott, T. D., et al. 2017, *Phys. Rev. Lett.*, **119**, 161101

[3] Abbott, B. P., Abbott, R., Abbott, T. D., et al. 2017, *Nature (London)*, **551**, 85

[4] Abbott, B. P., et al. 2017, *Astrophys. J. Lett.*, **848**, L13

[5] Abbott, B. P., Abbott, R., Abbott, T. D., et al. 2020, *The Astrophysical Journal Letters*, **892**, L3

[6] —. 2020, *Living Reviews in Relativity*, 23

[7] Abbott, R., et al. 2020, *Astrophys. J. Lett.*, **896**, L44

[8] Abbott, R., Abbott, T. D., Abraham, S., et al. 2021, *The Astrophysical Journal Letters*, **915**, L5

[9] Abbott, R., et al. 2023, *Physical Review X*, 13

[10] Abbott, R., Abbott, T. D., Acernese, F., et al. 2023, *Physical Review X*, **13**, 011048, aDS Bibcode: 2023PhRvX..13a1048A

[11] Acernese, F., et al. 2015, *Class. Quant. Grav.*, **32**, 024001

[12] Agathos, M., Zappa, F., Bernuzzi, S., et al. 2020, *Phys. Rev. D*, **101**, 044006

[13] Akutsu, T., et al. 2021, *PTEP*, **2021**, 05A101

[14] Anand, S., Coughlin, M. W., Kasliwal, M. M., et al. 2020, *Nature Astronomy*, **5**, 46–53

[15] Anand, S., Pang, P. T. H., Bulla, M., et al. 2023, Chemical Distribution of the Dynamical Ejecta in the Neutron Star Merger GW170817, *arXiv:2307.11080 [astro-ph.HE]*

[16] Andreoni, I., Goldstein, D. A., Kasliwal, M. M., et al. 2020, *Astrophys. J.*, **890**, 131

[17] Ashton, G., Ackley, K., Magaña Hernandez, I., & Piotrzkowski, B. 2020, arXiv e-prints, arXiv:2009.12346

[18] Barbieri, C., Salafia, O. S., Colpi, M., et al. 2019, *The Astrophysical Journal Letters*, **887**, L35

[19] Bardeen, J. M., Press, W. H., & Teukolsky, S. A. 1972, *Astrophys. J.*, **178**, 347

[20] Bauswein, A., Baumgarte, T. W., & Janka, H. T. 2013, *Phys. Rev. Lett.*, **111**, 131101

[21] Bauswein, A., Goriely, S., & Janka, H.-T. 2013, *The Astrophysical Journal*, **773**, 78

[22] Bauswein, A., Just, O., Janka, H.-T., & Stergioulas, N. 2017, *The Astrophysical Journal Letters*, **850**, L34

[23] Belgacem, E., Dirian, Y., Foffa, S., & Maggiore, M. 2018, *Physical Review D*, **98**

[24] Bhardwaj, M., Palmese, A., Hernandez, I. M., D’Emilio, V., & Morisaki, S. 2023, Challenges for Fast Radio Bursts as Multi-Messenger Sources from Binary Neutron Star Mergers, *arXiv:2306.00948 [astro-ph.HE]*

[25] Biscoveanu, S., Landry, P., & Vitale, S. 2022, *Monthly Notices of the Royal Astronomical Society*, **518**, 5298–5312

[26] Blanchard, P. K., Berger, E., Fong, W., et al. 2017, *The Astrophysical Journal*, **848**, L22

[27] Bom, C. R., Annis, J., Garcia, A., et al. 2024, *Astrophys. J.*, **960**, 122

[28] Breu, C., & Rezzolla, L. 2016, *Monthly Notices of the Royal Astronomical Society*, **459**, 646–656

[29] Bulla, M. 2019, *Monthly Notices of the Royal Astronomical Society*, **489**, 5037–5045

[30] Bulla, M., Coughlin, M. W., Dhawan, S., & Dietrich, T. 2022, *Universe*, **8**, 289

[31] Cabrera, T., Palmese, A., Hu, L., et al. 2024, Searching for electromagnetic emission in an AGN from the gravitational wave binary black hole merger candidate S230922g, *arXiv:2407.10698 [astro-ph.HE]*

[32] Collaboration, T. L. S., the Virgo Collaboration, the KAGRA Collaboration, et al. 2022, The population of merging compact binaries inferred using gravitational waves through GWTC-3, *arXiv:2111.03634 [astro-ph.HE]*

[33] Colombo, A., Salafia, O. S., Gabrielli, F., et al. 2022, *Astrophys. J.*, **937**, 79

[34] Colombo, A., Duqué, R., Salafia, O. S., et al. 2024, *Astronomy & Astrophysics*, **686**, A265

[35] Coughlin, M., & Stubbs, C. 2016, *Experimental Astronomy*, **42**, 165–178

[36] Coughlin, M. W., Dietrich, T., Doctor, Z., et al. 2018, *Monthly Notices of the Royal Astronomical Society*, **478**, 2890–2904

Notices of the Royal Astronomical Society, 480, 3871–3878

[37] Coughlin, M. W., Tao, D., Chan, M. L., et al. 2018, *Monthly Notices of the Royal Astronomical Society*, 478, 692–702

[38] Coulter, D. A., Foley, R. J., Kilpatrick, C. D., et al. 2017, *Science*, 358, 1556

[39] Dietrich, T., Coughlin, M. W., Pang, P. T. H., et al. 2020, *Science*, 370, 1450–1453

[40] Domoto, N., Tanaka, M., Wanajo, S., & Kawaguchi, K. 2021, *Astrophys. J.*, 913, 26

[41] Farah, A., Fishbach, M., Essick, R., Holz, D. E., & Galauadage, S. 2022, *The Astrophysical Journal*, 931, 108

[42] Fishbach, M., Essick, R., & Holz, D. E. 2020, *The Astrophysical Journal*, 899, L8

[43] Flaugher, B., Diehl, H. T., Honscheid, K., et al. 2015, *The Astronomical Journal*, 150, 150

[44] Fong, W., Blanchard, P. K., Alexander, K. D., et al. 2019, *The Astrophysical Journal Letters*, 883, L1

[45] Foucart, F., Hinderer, T., & Nissanke, S. 2018, *Physical Review D*, 98

[46] Gao, W.-H., & Fan, Y.-Z. 2006, *Chinese Journal of Astronomy and Astrophysics*, 6, 513

[47] Gill, R., Nathanail, A., & Rezzolla, L. 2019, *The Astrophysical Journal*, 876, 139

[48] Gomez, S., Hosseinzadeh, G., Cowperthwaite, P. S., et al. 2019, *The Astrophysical Journal Letters*, 884, L55

[49] Graham, M., Ford, K., McKernan, B., et al. 2020, *Physical Review Letters*, 124

[50] Hotokezaka, K., Kiuchi, K., Kyutoku, K., et al. 2013, *Physical Review D*, 87

[51] Hotokezaka, K., Kyutoku, K., Okawa, H., Shibata, M., & Kiuchi, K. 2011, *Physical Review D*, 83

[52] Hotokezaka, K., Nakar, E., Gottlieb, O., et al. 2019, *Nature Astronomy*, 3, 940

[53] Hotokezaka, K., Tanaka, M., Kato, D., & Gaigalas, G. 2023, *MNRAS*, 526, L155

[54] Huth, S., et al. 2022, *Nature*, 606, 276

[55] KAGRA Collaboration, LIGO Scientific Collaboration, & Virgo Collaboration. 2018, *Living Reviews in Relativity*, 21, 3

[56] Kalogera, V., & Baym, G. 1996, *The Astrophysical Journal*, 470, L61–L64

[57] Kasen, D., Metzger, B., Barnes, J., Quataert, E., & Ramirez-Ruiz, E. 2017, *Nature*, 551, 80–84

[58] Kaur, R., O’Connor, B., Palmese, A., & Kunnumkai, K. 2024, Detecting prompt and afterglow jet emission of gravitational wave events from LIGO/Virgo/KAGRA and next generation detectors, [arXiv:2410.10579 \[astro-ph.HE\]](https://arxiv.org/abs/2410.10579)

[59] Kawaguchi, K., Shibata, M., & Tanaka, M. 2020, *The Astrophysical Journal*, 889, 171

[60] Kiendrebeogo, R. W., Farah, A. M., Foley, E. M., et al. 2023, *The Astrophysical Journal*, 958, 158

[61] Kilpatrick, C. D., Fong, W.-f., Blanchard, P. K., et al. 2022, *The Astrophysical Journal*, 926, 49

[62] Krüger, C. J., & Foucart, F. 2020, *Physical Review D*, 101

[63] Kunnumkai, K., Palmese, A., Bulla, M., et al. 2024, *arXiv e-prints*, arXiv:2409.10651

[64] Kunnumkai, K., Palmese, A., & Farah, A. 2024, *Zenodo*

[65] Lattimer, J. M., & Prakash, M. 2001, *The Astrophysical Journal*, 550, 426–442

[66] LIGO Scientific Collaboration. 2018, LIGO Algorithm Library - LALSuite, free software (GPL)

[67] LIGO Scientific Collaboration, Virgo Collaboration, & KAGRA Collaboration. 2021, GWTC-3: Compact Binary Coalescences Observed by LIGO and Virgo During the Second Part of the Third Observing Run, [arXiv:2111.03606 \[gr-qc\]](https://arxiv.org/abs/2111.03606)

[68] LIGO Scientific Collaboration, Virgo Collaboration, GBM, F., et al. 2017, *The Astrophysical Journal Letters*, 848, L12

[69] Magaña Hernandez, I., d’Emilio, V., Morisaki, S., Bhardwaj, M., & Palmese, A. 2024, *The Astrophysical Journal Letters*, 971, L5

[70] Makhathini, S., Mooley, K. P., Brightman, M., et al. 2021, *The Astrophysical Journal*, 922, 154

[71] Margalit, B., & Metzger, B. D. 2017, *The Astrophysical Journal Letters*, 850, L19

[72] —. 2019, *The Astrophysical Journal Letters*, 880, L15

[73] Margutti, R., & Chornock, R. 2021, *Annual Review of Astronomy and Astrophysics*, 59, 155

[74] Mathias, L. W. P., Di Clemente, F., Bulla, M., & Alessandro, D. 2024, *MNRAS*, 527, 11053

[75] Metzger, B. D. 2019, *Living Reviews in Relativity*, 23, 1

[76] Metzger, B. D., Quataert, E., & Thompson, T. A. 2008, *Monthly Notices of the Royal Astronomical Society*, 385, 1455

[77] Moroianu, A., Wen, L., James, C. W., et al. 2023, *Nature Astronomy*, 7, 579

[78] Most, E. R., Papenfort, L. J., Weih, L. R., & Rezzolla, L. 2020, *MNRAS*, 499, L82

[79] Nakar, E. 2020, *Physics Reports*, 886, 1

[80] Ng, K. K., Vitale, S., Zimmerman, A., et al. 2018, *Physical Review D*, 98

[81] Nugent, A. E., Fong, W., Dong, Y., et al. 2020, *The Astrophysical Journal*, 904, 52

[82] Ofek, E. O., Strotjohann, N. L., Arcavi, I., et al. 2023, *Monthly Notices of the Royal Astronomical Society*, 527, 3741

[83] Palmese, A., Fishbach, M., Burke, C. J., Annis, J., & Liu, X. 2021, *The Astrophysical Journal Letters*, 914, L34

[84] Palmese, A., Kaur, R., Hajela, A., et al. 2024, *Phys. Rev. D*, 109, 063508

[85] Palmese, A., Hartley, W., Tarsitano, F., et al. 2017, *The Astrophysical Journal Letters*, 849, L34

[86] Pang, P. T. H., Dietrich, T., Coughlin, M. W., et al. 2023, *Nature Communications*, 14

[87] Petrov, P., Singer, L. P., Coughlin, M. W., et al. 2022, *The Astrophysical Journal*, 924, 54

[88] Piro, L., Troja, E., Zhang, B., et al. 2018, *Monthly Notices of the Royal Astronomical Society*, 483, 1912

[89] Pérez-García, M. A., Izzo, L., Barba-González, D., et al. 2022, *Astronomy & Astrophysics*, 666, A67

[90] Raaijmakers, G., et al. 2021, *Astrophys. J.*, 922, 269

[91] Radice, D., Riciglano, G., Bhattacharya, M., et al. 2024, *Monthly Notices of the Royal Astronomical Society*, 528, 5836–5844

[92] Rezzolla, L., & Kumar, P. 2015, *The Astrophysical Journal*, 802, 95

[93] Rosswog, S., Liebendörfer, M., Thielemann, F. K., et al. 1999, *Astronomy & Astrophysics*, 341, 499

[94] Rykoff, E. S., Rozo, E., Hollowood, D., et al. 2016, *The Astrophysical Journal Supplement*, 224, 1

[95] Sarin, N., Lasky, P. D., Vivanco, F. H., et al. 2022, *Physical Review D*, 105

[96] Shah, V. G., Narayan, G., Perkins, H. M. L., et al. 2024, *MNRAS*, 528, 1109

[97] Shibata, M., & Taniguchi, K. 2006, *Physical Review D*, 73

[98] Siegel, D. M., Ciolfi, R., Harte, A. I., & Rezzolla, L. 2013, *Physical Review D*, 87

[99] Singer, L. P., & Price, I. R. 2016, *Phys. Rev. D*, 93, 024013

[100] Singer, L. P., Chen, H.-Y., Holz, D. E., et al. 2016, *The Astrophysical Journal*, 829, L15

[101] Smartt, S. J., Nicholl, M., Srivastav, S., et al. 2023,

GW190425: Pan-STARRS and ATLAS coverage of the skymap and limits on optical emission associated with FRB190425, [arXiv:2309.11340 \[astro-ph.HE\]](https://arxiv.org/abs/2309.11340)

[102] Sneppen, A., & Watson, D. 2023, *Astronomy & Astrophysics*, **675**, A194

[103] Soares-Santos, M., Holz, D. E., Annis, J., et al. 2017, *The Astrophysical Journal*, **848**, L16

[104] Tsai, Y.-D., Palmese, A., Profumo, S., & Jeltema, T. 2021, *JCAP*, **2021**, 019

[105] Vieira, N., Ruan, J. J., Haggard, D., et al. 2023, *Astrophys. J.*, **944**, 123

[106] Watson, D., Hansen, C. J., Selsing, J., et al. 2019, *Nature (London)*, **574**, 497

[107] Yu, Y.-W., Liu, L.-D., & Dai, Z.-G. 2018, *The Astrophysical Journal*, **861**, 114

[108] Zhang, B., & Mészáros, P. 2001, *The Astrophysical Journal*, **552**, L35

[109] Zhao, C., Lu, Y., Chu, Q., & Zhao, W. 2023, *Monthly Notices of the Royal Astronomical Society*, **522**, 912–936

[110] Zhu, X., Thrane, E., Osłowski, S., Levin, Y., & Lasky, P. D. 2018, *Phys. Rev. D*, **98**, 043002